Accepted Manuscript
Version of record at: https://doi.org/10.1109/TGRS.2022.3202567

Multi-channel Signal Modeling and AMTI Performance Analysis for Distributed Space-based Radar Systems

Jiangyuan Chen, Penghui Huang *Member, IEEE*, Xiang-Gen Xia, *Fellow, IEEE*, Junli Chen, Yongyan Sun, Xingzhao Liu, *Member, IEEE*, and Guisheng Liao, *Senior Member, IEEE*

***Abstract*—Due to the limited size, carrying capacity, power-aperture product, and high hardware cost of satellite platform, the traditional single-platform spaceborne radar system encounters the problems of poor target minimum detectable velocity (MDV) performance, considerably deteriorating the moving target detection performance. To improve the air moving target indication (AMTI) performance, especially for a weak target, distributed space-based radar system (DSBR) becomes a good candidate due to the longer along-track baseline (ATB) and spatial power synthesis. However, due to the sparse configuration of radar baseline distribution, the detection performance of air moving targets (AMTs) will be restricted by many practical factors in an actual DSBR system. In this paper, multi-channel signal models of an observed moving target and ground clutter are accurately established in a DSBR framework, where the error influences of cross-track baseline (CTB), terrain fluctuation, and channel inconsistency response are considered. Then, the influence of the non-ideal factors, including the channel noise, long-intersatellite ATB, long-intersatellite CTB, synchronization errors, and interchannel amplitude and phase inconsistency errors, on the AMTI performance is analyzed term by term. The simulation results provide the useful guidance for the system design of a DSBR with the AMTI tasks.**

***Index Terms*—Distributed space-based early warning radar (DSBR), air moving target indication (AMTI), space-time adaptive processing (STAP), interchannel correlation analysis.**

I. Introduction

In recent years, the detection of air moving targets (AMTs) faces many challenges, such as the difficulty in long-time and long-distance surveillance, the detection difficulty of AMTs with a small radar cross-section (RCS), and strong clutter interference. Therefore, how to realize the effective detection of AMTs has been an active research topic. Usually, ground-based radar [1]-[4] and airborne radar systems [5]-[7] can be used to effectively detect AMTs with a relatively short detection distance. However, the air moving target indication (AMTI) ability of a ground-based radar may be limited by the influences of ground object occlusion and earth curvature [8]-[10]. In addition, an airborne radar system may be restricted by climate change and country airspace boundaries [11], [12]. To deal with these problems, the development of space-based radar system (SBR) becomes necessity, which can effectively break through the space restrictions of the terrain occlusion, and the time limitation brought by the atrocious climate and weather, significantly improving the radar wide-area detection, tracking, and localization performances of an AMT [13]. Therefore, the farther surveillance range, longer warning time, and higher detection accuracy can be obtained in an SBR system.

For an SBR system, due to its downward-looking surveillance mode, a large number of strong ground clutter echoes will be received by the radar receiver. Besides, due to the high-speed motion of spaceborne platform, Doppler spectrum of the main-lobe clutter is severely broadened, dramatically decreasing the output signal-to-clutter and noise ratio (SCNR) of a moving target. Therefore, in order to realize the reliable detection of AMTs, the effective clutter suppression becomes necessary. For the broadened ground clutter, the multichannel processing technology is an effective approach to accomplish the main-lobe clutter cancellation by exploiting the clutter space-time coupling characteristics, and a typical technique is space-time adaptive processing (STAP)[14]-[17]. According to the corresponding relationship between the Doppler frequencies and cone angles of the observed scene scatterers, STAP technology makes full use of spatial and temporal two-dimensional degrees of freedom (DOF) to suppress the strong main-lobe clutter. Although the full-dimensional STAP has excellent clutter suppression performance, it is hard to realize the on-board and real-time clutter cancellation processing due to the high computational complexity. Moreover, the inhomogeneous and non-stationary characteristics of clutter are other important factors restricting the practical applications of STAP. To solve these issues, there are many STAP algorithms in the literature, see, for example, [18]-[36].

However, for a single-platform SBR system, although some advanced signal processing techniques can be applied to enhance the signal processing gain, the AMTI performance is still restricted by the system power-aperture product and along-track baseline (ATB) length [37], resulting in unsatisfied target velocity response performance, especially for aerocraft targets with relatively slow speed. Therefore, a

Manuscript received June 14, 2022; revised August 5, 2022; accepted August 21, 2022. This work was supported in part by the National Natural Science Foundation Program of China under Grant 62171272, in part by the USCAST2021-15. (*Corresponding author: Penghui Huang*)

Jiangyuan Chen, Penghui Huang, and Xingzhao Liu are with the School of Electronic Information and Electrical Engineering, Shanghai Jiao Tong University, Shanghai 200240, China (e-mail: c532021803@sjtu.edu.cn; huangpenghui@sjtu.edu.cn; xzhliu@sjtu.edu.cn).

Xiang-Gen Xia is with the College of Communications Engineering, Xidian University, Xi'an 710071, China, and also with the Department of Electrical and Computer Engineering, University of Delaware, Newark, DE 19716, USA (e-mail: xxia@ee.udel.edu).

Guisheng Liao is with the National Laboratory of Radar Signal Processing, Xidian University, Xi'an 710071, China (e-mail: liaogs@xidian.edu.cn).

Junli Chen and Yongyan Sun are with the Shanghai Satellite Engineering Research Institute, Shanghai 201109, China (e-mail: chen090068@163.com; yanr0729@hotmail.com).

new radar framework is needed to deal with the antenna size limitation. To do so, a distributed satellite radar system permits a huge but sparse antenna aperture by controlling multiple satellites to work together to significantly improve the AMTI performance because of its precious ATB resource, thus becomes a good candidate in the new-generation anti-stealth system.

As a new space-based radar framework, the baseline configuration of a distributed satellite radar system [38]-[40] can be flexibly adjusted to meet different mission requirements, such as moving target detection and elevation interferometry, through formation configuration and control. To implement the AMTI mission, the satellites of a DSBR system should be arranged along the track [41]. The formation flight mode in a distributed satellite system can provide longer ATB and larger spatial DOF, and thus improve the AMTI performance via spatial power synthesis and adaptive clutter filtering [40][42]. Besides, the flexible combinations of multi-station and multi-phase centers make it possible accomplish more accurate target relocation tasks [40]. These advantages make the distributed radar system become the development focus of the next-generation spaceborne radar.

However, the AMTI performance of a distributed space-based early warning radar (DSBR) system is affected by many practical factors. Although the along-track observation configuration is the optimal configuration for AMTI [55], in a real distributed system, in order to minimize satellite collision risks [58], economize orbital energy [59], and take full advantage of the adjustable spatial baseline of a DSBR system to perform multiple tasks, such as synthetic aperture radar interferometry (InSAR) [60], the pure along-track baseline arrangement mode is not usually chosen for orbit design in a DSBR system. Taking some classical configurations, such as Helix formation [60] and Pendulum formation [62], for example, the main and auxiliary satellites are located at different orbits with an intended cross-track baseline (CTB). Due to the existence of CTB, an elevation angle deviation between the different satellites may cause clutter scattering spectrum of different satellites relatively offset along elevation dimension [43]. In addition, the existence of CTB will cause an additional phase term related to the elevation angle, which will destroy the independent identically distributed (i.i.d.) condition of clutter distribution, resulting in the clutter range-dependence. Additionally, when the undulating terrain appears, the CTB is very sensitive to the terrain fluctuation, further decreasing the channel correlation of clutter echoes.

Moreover, when multiple satellites work together in a DSBR system, due to the limited satellite attitude control precision, the space synchronization error inevitably exists [44][45]. Different frequency sources between the transmitting and receiving satellites in a DSBR system will introduce the frequency synchronization error [46][47]. Different clock sources of receiving and transmitting satellites will cause the inconsistent trigger pulses, resulting in time synchronization error [48][49]. The interchannel amplitude and phase errors are also unavoidable in practice [50][51]. Therefore, due to the existences of these non-ideal factors, the radar echo correlation among different channels in a DSBR system will decrease, which severely degrades the AMTI ability.

In order to analyze the AMTI capability in a DSBR system, we firstly establish the AMT signal model and clutter signal model with the considerations of the ATB, CTB, and terrain fluctuation. Then, the interferometric phase is selected to analyze the influences of CTB and terrain fluctuation on echo signal space-time property and multi-channel clutter suppression performance. Next, from the standpoint of echo correlation, the effects of ATB, CTB, synchronization errors, and interchannel amplitude and phase errors on interchannel correlation and target minimum detectable velocity (MDV) performance are analyzed in details. Finally, the simulation experiments are conducted to analyze the above non-ideal factors term by term.

The remainder of this paper is as follows. In Section II, moving target and clutter echo signal models in a DSBR system are introduced. In Section III, the effects of the channel noise, ATB, CTB, synchronization errors, and interchannel amplitude and phase errors on interchannel correlation are analyzed. In Section IV, the influence of the above non-ideal factors on MDV performance is analyzed through simulation experiments in details, providing reference for the design of the new-generation spaceborne surveillance systems with the AMTI tasks.

II. Received Signal Model

A. Target Signal Model in A DSBR System

For convenience, assume that a DSBR system has two satellites, where the main satellite transmits radar pulse signals and both the main satellite and the auxiliary satellite receive the backscattered returns, simultaneously. For this distributed satellite system, the antenna sizes of two satellites are assumed to be the same and each antenna is equally divided into N equivalent spatial subarrays along the azimuth dimension, as shown in Fig. 1, where an air moving target is located at position (x_t, y_t, z_t) in an *O-XYZ* Cartesian coordinate, with the *Y-axis* denoting the radar motion trajectory with an along-track velocity of V_a, *Z-axis* is perpendicular to the geoid and the *X-axis* is determined by the right-hand rule. A mixed baseline $B=\sqrt{B_x^2+B_y^2+B_z^2}$ between the main satellite and auxiliary satellites is present, where B_x, B_y, and B_z denote the baseline components along *X-axis*, *Y-axis*, and *Z-axis*, respectively. In this 3-D configuration, B_y represents the ATB, B_x and B_z are the CTB components along *X-axis* and *Z-axis*, respectively. The angles $\theta_{EL,t}$ and $\theta_{AZ,t}$ denote, respectively, the elevation angle and azimuth angle of the observed target relative to the main satellite. The first channel positions of the main satellite and auxiliary satellite are, respectively, denoted by $(0,0,H)$ and $(B_x, B_y, H+B_z)$, where H denotes the platform height.

Suppose that a linear frequency modulated (LFM) signal is adopted as the baseband waveform transmitted by the main satellite, i.e.,

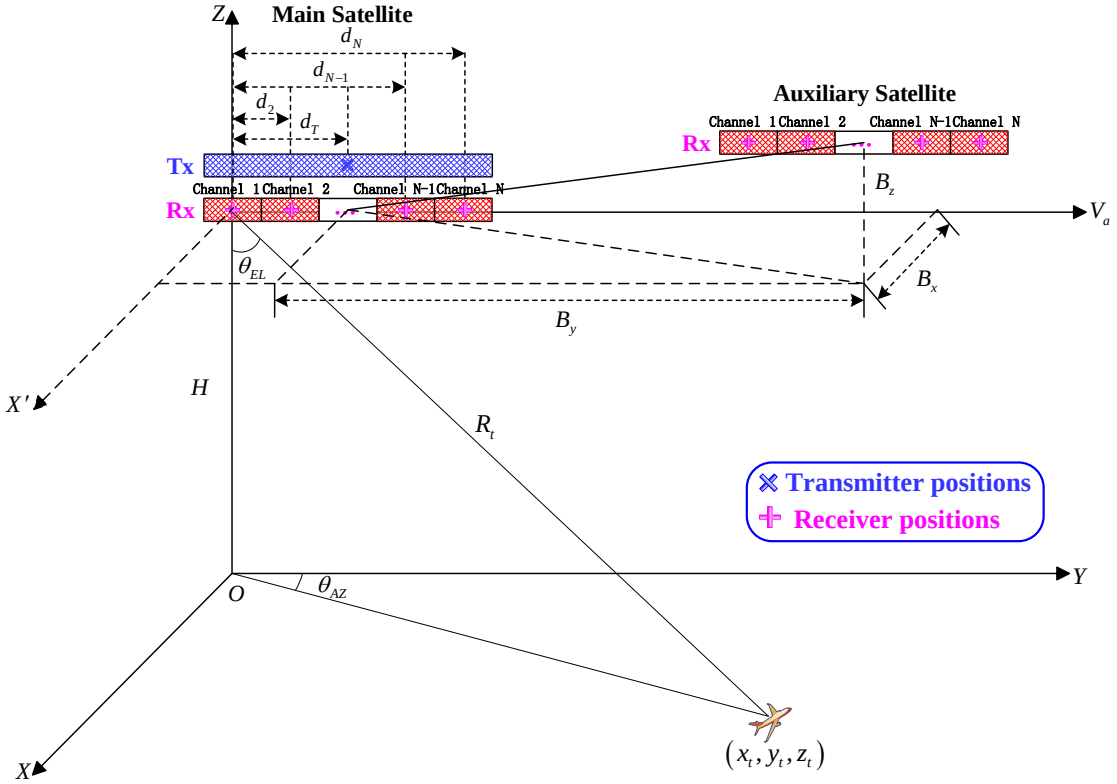

Fig. 1 Geometry between the DSBR system and an air moving target.

$$s_T(t) = rect\left(\frac{t}{T_P}\right)\exp(j\pi Kt^2)\exp(j2\pi f_0 t) \tag{1}$$

where $rect(\cdot)$ is a rectangular window function, t, T_P, K, f_0 represent the fast time variable, the pulse duration, the chirp rate of transmitted waveform, and the central frequency, respectively.

Assume that the initial position of an air moving target is (x_t, y_t, z_t), and the velocity components along the *X*-axis and *Y*-axis are, respectively, denoted by v_x and v_y, according to Fig. 1. Then the target echo signal of the *n*th channel, $n = 1, 2, ..., N$, in the main satellite and auxiliary satellite after range compression and down modulation can be expressed as

$$\begin{aligned} s_{sr,i,n}(t, t_m) = \sigma_{s,i}\omega_{az,i,n}(t_m)\,\mathrm{sinc}\left[B\left(t - \frac{2R_{s,i,n}(t_m)}{c}\right)\right] \\ \times \exp\left[-j\frac{4\pi}{\lambda}R_{s,i,n}(t_m)\right] \end{aligned} \tag{2}$$

where *i*=1 represents the main satellite and *i*=2 represents the auxiliary satellite. $\sigma_{s,i}$, B, λ, c and t_m represent the target signal amplitude after range compression, the signal bandwidth, the signal wavelength, the speed of light, and the azimuth slow-time variable, respectively. $\omega_{az,i,n}(t_m)$, represents the azimuth window function of the *n*th receiving channel in the main satellite and auxiliary satellites. $R_{s,1,n}(t_m)$ represents the two-way instantaneous slant-range from the nth spatial received channel of the main satellite to this AMT and $R_{s,2,n}(t_m)$ denotes the two-way instantaneous slant-range between the *n*th spatial received channel of the auxiliary satellite and the AMT. According to the radar equation, $\sigma_{s,i}$, can be expressed as

$$\sigma_{s,1} = \sqrt{\frac{P_{av}BG_{T0}G_{R0,1}\lambda^2 G_t(\theta_{AZ,t,1},\theta_{EL,t,1})G_r(\theta_{AZ,t,1},\theta_{EL,t,1})\cdot RCS\cdot PRT}{(4\pi)^3 R_t^4 L_s}} \tag{3}$$

$$\sigma_{s,2} = \sqrt{\frac{P_{av}BG_{T0}G_{R0,2}\lambda^2 G_t(\theta_{AZ,t,1},\theta_{EL,t,1})G_r(\theta_{AZ,t,2},\theta_{EL,t,2})\cdot RCS\cdot PRT}{(4\pi)^3 R_t^4 L_s}} \tag{4}$$

where $G_t(\theta_{AZ,t,1},\theta_{EL,t,1})$ and $G_r(\theta_{AZ,t,i},\theta_{EL,t,i})$, represent the normalized transmitting and receiving antenna patterns of this target relative to the beam center, respectively. The angles $\theta_{EL,t,1}$ and $\theta_{AZ,t,1}$ denote, respectively, the elevation angle and azimuth angle of the observed target relative to the main satellite. And the angles $\theta_{EL,t,2}$ and $\theta_{AZ,t,2}$ represent, respectively, the elevation angle and azimuth angle of the observed target relative to the auxiliary satellite. P_{av}, PRT, G_{T0}, $G_{R0,i}$, RCS, and L_s denote the radar average transmitting power, pulse repetition time, antenna transmitting gain, antenna receiving gain, target radar cross section (RCS), and system loss, respectively, where the radar system loss includes the waveguide equipment wear and tear, atmospheric propagation loss, antenna beam shape loss, signal processing loss, etc.

According to Fig. 1, the two-way instantaneous slant-range between the *n*th spatial received channel of the main and auxiliary satellites and an AMT can be expressed as:

$$R_{s,1,n}(t_m)=\frac{1}{2}\left(\begin{array}{l}\sqrt{\left(x_t+v_xt_m\right)^2+\left(H-z_t\right)^2}\\ \quad+\left((N-1)d/2+V_at_m-y_t-v_yt_m\right)^2\\ +\sqrt{\left(x_t+v_xt_m\right)^2+\left(H-z_t\right)^2}\\ \quad+\left((n-1)d+V_at_m-y_t-v_yt_m\right)^2\end{array}\right) \quad (5)$$

$$R_{s,2,n}(t_m)=\frac{1}{2}\left(\begin{array}{l}\sqrt{\left(x_t+v_xt_m\right)^2+\left(H-z_t\right)^2}\\ \quad+\left((N-1)d/2+V_at_m-y_t-v_yt_m\right)^2\\ +\sqrt{\left(B_x-x_t-v_xt_m\right)^2+\left(H+B_z-z_t\right)^2}\\ \quad+\left((n-1)d+B_y+V_at_m-y_t-v_yt_m\right)^2\end{array}\right) \quad (6)$$

According to the equivalent phase center principle [52], the slant-range histories of the main and auxiliary satellites are, respectively, equivalent to

$$R_{s,1,n}(t_m)\approx\sqrt{\left(x_t+v_xt_m\right)^2+\left(d_{pc\_n}+V_at_m-y_t-v_yt_m\right)^2+\left(H-z_t\right)^2} \quad (7)$$

$$R_{s,2,n}(t_m)\approx\sqrt{\begin{array}{l}\left(\frac{B_x}{2}-x_t-v_xt_m\right)^2+\left(H+\frac{B_z}{2}-z_t\right)^2\\ \quad+\left(d_{pc\_n}+\frac{B_y}{2}+V_at_m-y_t-v_yt_m\right)^2\end{array}} \quad (8)$$

where $d_{pc\_n}=\frac{N-3}{4}d+\frac{n}{2}d$ denotes the azimuth position of the equivalent phase center of the *n*th spatial channel in the main and auxiliary satellites. $v_r=\frac{x_t}{R_t}v_x+\frac{y_t}{R_t}v_y$ represents the radial velocity of this AMT and $R_t=\sqrt{x_t^2+y_t^2+H^2}$ denotes the nearest slant range.

According to the second-order Taylor expansion, (7) and (8) can be, respectively, expanded as

$$\begin{aligned}R_{s,1,n}(t_m)\approx{}&R_t+v_rt_m-\left(d_{pc\_n}+V_at_m\right)\cos\theta_{cone,t}+\frac{z_t^2-2Hz_t}{2R_t}\\&+\frac{\left(d_{pc\_n}+V_at_m-v_yt_m\right)^2}{2R_t}+\frac{v_x^2t_m^2}{2R_t}\\&-\frac{R_t}{8}\left[\begin{array}{l}\frac{2v_rt_m}{R_t}-\frac{2y_t}{R_t^2}\left(d_{pc\_n}+V_at_m\right)+\frac{z_t^2-2Hz_t}{R_t^2}\\ \quad+\frac{\left(d_{pc\_n}+V_at_m-v_yt_m\right)^2}{R_t^2}+\frac{v_x^2t_m^2}{R_t^2}\end{array}\right]^2\end{aligned} \quad (9)$$

$$\begin{aligned}R_{s,2,n}(t_m)\approx{}&R_t+v_rt_m-\frac{B_xv_xt_m}{2R_t}-\frac{B_yv_yt_m}{2R_t}+\frac{z_t^2-2Hz_t}{2R_t}-\frac{B_xx_t}{2R_t}\\&-\left(d_{pc\_n}+V_at_m\right)\cos\theta_{cone,t}+\frac{B_y}{2R_t}\left(d_{pc\_n}+V_at_m\right)\\&-\frac{B_yy_t}{2R_t}+\frac{B_zH}{2R_t}-\frac{B_zz_t}{2R_t}+\frac{B^2}{8R_t}\\&+\frac{\left(d_{pc\_n}+V_at_m-v_yt_m\right)^2}{2R_t}+\frac{v_x^2t_m^2}{2R_t}\\&-\frac{R_t}{8}\left[\begin{array}{l}\frac{2v_rt_m}{R_t}-\frac{B_xv_xt_m}{R_t^2}-\frac{B_yv_yt_m}{R_t^2}+\frac{z_t^2-2Hz_t}{R_t^2}\\ \quad+\frac{B_y-2y_t}{R_t^2}\left(d_{pc\_n}+V_at_m\right)-\frac{B_xx_t}{R_t^2}\\ \quad-\frac{B_yy_t}{R_t^2}+\frac{B_zH}{R_t^2}-\frac{B_zz_t}{R_t^2}+\frac{B^2}{4R_t^2}\\ \quad+\frac{\left(d_{pc\_n}+V_at_m-v_yt_m\right)^2}{R_t^2}+\frac{v_x^2t_m^2}{R_t^2}\end{array}\right]^2\end{aligned} \quad (10)$$

where $\cos\theta_{cone,t}=\sin\theta_{EL,t}\cos\theta_{AZ,t}$ represents the cone angle of this observed target relative to the main satellite.

Usually, in an SBR system, the target dwell time is about 20~50 ms [53][54] under the restrictions of coverage rate requirement and data rate restriction, so the target range migration effect can be ignored and the second-order phase can be approximately compensated by using the *priori* radar system parameters, with the compensation function as

$$H_{match}\left(t_m\right)=rect\left(\frac{t_m}{T_a}\right)\exp\left\{-j\frac{2\pi}{\lambda}\cdot\frac{V_a^2t_m^2}{R_t}\right\} \quad (11)$$

Considering that $V_at_m\ll R_t$ and $B\ll R_t$ hold, the target radar returns of the main and auxiliary satellites can be further approximated in (12) and (13) shown in the next page.

It can be seen from (12) and (13) that the instantaneous Doppler frequencies of the *n*th channels of the main and auxiliary satellites can be, respectively, expressed as

$$f_{ds,1,n}=\left(1-\frac{z_t^2-2Hz_t}{2R_t^2}\right)\left(\frac{2v_r}{\lambda}-\frac{2V_a\cos\theta_{cone,t}}{\lambda}+\frac{2d_{pc\_n}\left(V_a-v_y\right)}{\lambda R_t}\right) \quad (14)$$

$$f_{ds,2,n}=\left(1-\frac{z_t^2-2Hz_t}{2R_t^2}\right)\left(\begin{array}{l}\frac{2v_r}{\lambda}-\frac{2V_a\cos\theta_{cone,t}}{\lambda}+\frac{B_yV_a}{\lambda R_t}\\ -\frac{B_xv_x}{\lambda R_t}-\frac{B_yv_y}{\lambda R_t}+\frac{2d_{pc\_n}\left(V_a-v_y\right)}{\lambda R_t}\end{array}\right) \quad (15)$$

From (14) and (15), it can be seen that, the target Doppler center frequency is related to the terrain altitude, ATB length, wave length, platform velocity, and target velocity. Besides, one can see that, the registration error terms, i.e., $\frac{2d_{pc\_n}\left(V_a-v_y\right)}{\lambda R_t}$, in the main satellite and

$\frac{2d_{pc\_n}\left(V_a-v_y\right)}{\lambda R_t}+\frac{B_yV_a}{\lambda R_t}-\frac{B_xv_x}{\lambda R_t}-\frac{B_yv_y}{\lambda R_t}$ in the auxiliary satellite exist. Due to the long ATB of a distributed spaceborne radar system, the registration error may be easily larger than an azimuth resolution cell, which will considerably degrade the AMTI and target location performances.

B. Clutter Signal Model in A DSBR System

For the same reason, as for the ground scattering point *P* located at (x_c, y_c, z_c), the clutter echo signals of the *n*th

$$s_{sr,1,n}(t,t_m)\approx\sigma_{s,1}\,\mathrm{sinc}\left[B\left(t-\frac{2R_t}{c}\right)\right]rect\left(\frac{t_m}{T_a}\right)\exp\left\{-j\frac{4\pi}{\lambda}\left[R_t-\left(1-\frac{z_t^2-2Hz_t}{2R_t^2}\right)d_{pc\_n}\cos\theta_{cone,t}\right]\right\}\exp\left(j\phi_{z_t}\right)$$
$$\times rect\left(\frac{t_m+\left(n-1\right)d\Big/2V_a}{T_a}\right)\exp\left\{-j\frac{4\pi}{\lambda}\left(1-\frac{z_t^2-2Hz_t}{2R_t^2}\right)\left(v_rt_m-V_at_m\cos\theta_{cone,t}+\frac{d_{pc\_n}\left(V_a-v_y\right)t_m}{R_t}\right)\right\} \quad (12)$$

where $\phi_{z_t}=-\frac{2\pi}{\lambda}\left[\frac{z_t^2-2Hz_t}{R_t}-\frac{\left(z_t^2-2Hz_t\right)^2}{4R_t^3}\right]$.

$$s_{sr,2,n}(t,t_m)\approx\sigma_{s,2}\,\mathrm{sinc}\left[B\left(t-\frac{2R_t}{c}\right)\right]rect\left(\frac{t_m+\left(n-1\right)d+B_y\Big/2V_a}{T_a}\right)rect\left(\frac{t_m}{T_a}\right)\exp\left(j\phi_{z_t}\right)\exp\left(j\phi_{CTB,t}\right)$$
$$\times\exp\left\{-j\frac{4\pi}{\lambda}\left[R_t-\left(1-\frac{z_t^2-2Hz_t}{2R_t^2}\right)\times\left(d_{pc\_n}\cos\theta_{cone,t}+\frac{B_y}{2}\cos\theta_{cone,t}\right)\right]\right\} \quad (13)$$
$$\times\exp\left\{-j\frac{4\pi}{\lambda}\left(1-\frac{z_t^2-2Hz_t}{2R_t^2}\right)\left(v_rt_m-V_at_m\cos\theta_{cone,t}+\frac{d_{pc\_n}\left(V_a-v_y\right)t_m}{R_t}+\frac{B_y\left(V_a-v_y\right)t_m}{2R_t}-\frac{B_xv_xt_m}{2R_t}\right)\right\}$$

where T_a represents the coherent integration time.

$$\phi_{CTB,t}=-\frac{4\pi}{\lambda}\left[\left(1-\frac{z_t^2-2Hz_t}{2R_t^2}\right)\left(\frac{B^2}{8R_t}-\frac{B_xx_t}{2R_t}+\frac{B_zH}{2R_t}-\frac{B_zz_t}{2R_t}\right)\right]+\frac{\pi}{2\lambda R_t^3}\left(-B_xx_t-B_yy_t+B_zH-B_zz_t\right)$$
$$+\frac{\pi B^2}{4\lambda R_t^3}\left(-B_xx_t-B_yy_t+B_zH-B_zz_t\right).$$

$$s_{cr,1,n}(t,t_m)\approx\sigma_{c,1}\,\mathrm{sinc}\left[B\left(t-\frac{2R_c}{c}\right)\right]rect\left(\frac{t_m}{T_a}\right)\exp\left(j\phi_{z_c}\right)\exp\left\{-j\frac{4\pi}{\lambda}\left[R_c-\left(1-\frac{z_c^2-2Hz_c}{2R_c^2}\right)d_{pc\_n}\cos\theta_{cone,c}\right]\right\}$$
$$\times rect\left(\frac{t_m+\left(n-1\right)d\Big/2V_a}{T_a}\right)\exp\left\{-j\frac{4\pi}{\lambda}\left(1-\frac{z_c^2-2Hz_c}{2R_c^2}\right)\left(-V_at_m\cos\theta_{cone,c}+\frac{d_{pc\_n}V_at_m}{R_c}\right)\right\} \quad (16)$$

Where $\sigma_{c,1}=\sqrt{\frac{P_{av}BG_{T0}G_{R0,1}\lambda^2\cdot PRT}{\left(4\pi\right)^3R_c^4}\cdot\frac{\sigma_0\rho_r\rho_a}{\cos\psi}\cdot\frac{G_t\left(\theta_{AZ,c,1},\theta_{EL,c,1}\right)G_r\left(\theta_{AZ,c,1},\theta_{EL,c,1}\right)}{L_s}}$ denote the clutter signal amplitudes after performing the range compression with respect to the main satellite. σ_0, ρ_r, ρ_a, and ψ represent the clutter backscattering coefficient, range resolution, azimuth resolution, and grazing angle, respectively, where the clutter backscattering coefficient can be portrayed by the Morchin model [69]. $G_t\left(\theta_{AZ,c,i},\theta_{EL,c,i}\right)$ and $G_r\left(\theta_{AZ,c,i},\theta_{EL,c,i}\right)$, represent the normalized transmitting and receiving antenna patterns of the ground scattering point *P* relative to the beam center, respectively. The angles $\theta_{EL,c,1}$ and $\theta_{AZ,c,1}$ denote, respectively, the elevation angle and azimuth angle of *P* relative to the main satellite with $\cos\theta_{cone,c}=\sin\theta_{EL,c,1}\cos\theta_{AZ,c,1}$ corresponding to the cone angle. $R_c=\sqrt{x_c^2+y_c^2+H^2}$ denotes the nearest slant range. $\phi_{z_c}=-\frac{2\pi}{\lambda}\left[\frac{z_c^2-2Hz_c}{R_c}-\frac{\left(z_c^2-2Hz_c\right)^2}{4R_c^3}\right]$.

channel, in the main and auxiliary satellites after range compression and down modulation can be, respectively, expressed in (16) shown in the previous page and (17) below.

It can be seen from (16) and (17) that the instantaneous Doppler frequencies of the *n*th channels of the main and auxiliary satellites can, be respectively, expressed as

$$f_{dc,1,n}=\left(1-\frac{z_c^2-2Hz_c}{2R_c^2}\right)\left(-\frac{2V_a\cos\theta_{cone,c}}{\lambda}+\frac{2d_{pc\_n}V_a}{\lambda R_c}\right) \quad (18)$$

$$f_{dc,2,n}=\left(1-\frac{z_c^2-2Hz_c}{2R_c^2}\right)\left(-\frac{2V_a\cos\theta_{cone,c}}{\lambda}+\frac{2d_{pc\_n}V_a}{\lambda R_c}+\frac{B_yV_a}{\lambda R_c}\right) \quad (19)$$

By comparing (18) and (19), one can see that the clutter Doppler center frequency difference between the *n*th receiving channels of the main and auxiliary satellites can be calculated as $\left(1-\frac{z_c^2-2Hz_c}{2R_c^2}\right)\frac{B_yV_a}{\lambda R_c}$. In addition, the clutter Doppler center frequency difference between the *n*th receiving channel and the *m*th receiving channel in a single satellite can be obtained as $\left(1-\frac{z_c^2-2Hz_c}{2R_c^2}\right)\frac{|n-m|d\cdot V_a}{\lambda R_c}$. Obviously, due to the azimuth registration error caused by B_y in a DSBR system, the clutter returns of the different spatial channels in the main and auxiliary satellites are severely decorrelated, resulting in clutter suppression performance deterioration. In addition, according to (17), when two cross-track baselines B_x and B_z co-exist, the terrain fluctuation may further degrade the clutter spatial filtering ability.

C. Influences of CTB and Terrain Altitude on Clutter Suppression and AMTI Performance

After performing the azimuth FFT on (12) and (13), the target returns of the main and auxiliary satellites in the range-Doppler domain can be, respectively, noted in (20) below and (21) shown in the next page.

In the same way, the clutter returns of the main and auxiliary satellites in the range-Doppler domain can be, respectively, deduced in (22) and (23) shown in the next page.

By comparing (22) and (23), it can be seen that an interference phase ϕ exists between the receiving echoes of the main and auxiliary satellites, which can be written as

$$\phi=\phi_{CTB,c}+2\pi\left(1-\frac{z_c^2-2Hz_c}{2R_c^2}\right)\frac{B_yy_c}{\lambda R_c} \quad (24)$$

After ignoring the higher-order terms, the interference phase can be simplified as

$$\phi=-2\pi\left(1-\frac{z_c^2-2Hz_c}{2R_c^2}\right)\left(-\frac{B_xx_c}{\lambda R_c}-\frac{B_yy_c}{\lambda R_c}+\frac{B_zH}{\lambda R_c}-\frac{B_zz_c}{\lambda R_c}\right) \quad (25)$$

From (25), one can see that, the interference phase ϕ is related to ATB, CTB, slant-range of clutter component, range

---

$$\begin{aligned}s_{cr,2,n}(t,t_m)\approx\sigma_{c,2}\,\mathrm{sinc}\left[B\left(t-\frac{2R_c}{c}\right)\right]rect\left(\frac{t_m+\left(n-1\right)d+B_y\big/2V_a}{T_a}\right)rect\left(\frac{t_m}{T_a}\right)\exp\left(j\phi_{z_c}\right)\exp\left(j\phi_{CTB,c}\right)\\ \times\exp\left\{-j\frac{4\pi}{\lambda}\left[R_c-\left(1-\frac{z_c^2-2Hz_c}{2R_c^2}\right)\left(d_{pc\_n}\cos\theta_{cone,c}+\frac{B_y}{2}\cos\theta_{cone,c}\right)\right]\right\}\\ \times\exp\left\{-j\frac{4\pi}{\lambda}\left(1-\frac{z_c^2-2Hz_c}{2R_c^2}\right)\left(-V_at_m\cos\theta_{cone,c}+\frac{d_{pc\_n}V_at_m}{R_c}+\frac{B_yV_at_m}{2R_c}\right)\right\}\end{aligned} \quad (17)$$

where $\sigma_{c,2}=\sqrt{\frac{P_{av}BG_{T0}G_{R0,2}\lambda^2\cdot PRT}{\left(4\pi\right)^3R_c^4}\cdot\frac{\sigma_0\rho_r\rho_a}{\cos\psi}\cdot\frac{G_t\left(\theta_{AZ,c,1},\theta_{EL,c,1}\right)G_r\left(\theta_{AZ,c,2},\theta_{EL,c,2}\right)}{L_s}}$ denote the clutter signal amplitudes after performing the range compression with respect to the auxiliary satellite. And the angles $\theta_{EL,c,2}$ and $\theta_{AZ,c,2}$ represent, respectively, the elevation angle and azimuth angle of *P* relative to the auxiliary satellite.

$$\begin{aligned}\phi_{CTB,c}=&-\frac{4\pi}{\lambda}\left[\left(1-\frac{z_c^2-2Hz_c}{2R_c^2}\right)\left(\frac{B^2}{8R_c}-\frac{B_xx_c}{2R_c}+\frac{B_zH}{2R_c}-\frac{B_zz_c}{2R_c}\right)\right]+\frac{\pi}{2\lambda R_c^3}\left(-B_xx_c-B_yy_c+B_zH-B_zz_c\right)^2\\ &+\frac{\pi B^2}{4\lambda R_c^3}\left(-B_xx_c-B_yy_c+B_zH-B_zz_c\right)\end{aligned}.$$

$$\begin{aligned}s_{sr,1,n}(t,f_a)\approx&\left(1-\frac{\left(n-1\right)d}{2V_aT_a}\right)G_{azi}\sigma_{s,1}\exp\left\{j\frac{2\pi}{\lambda}\left(1-\frac{z_t^2-2Hz_t}{2R_t^2}\right)\left(n-1\right)d\cos\theta_{cone,t}\right\}\exp\left(j\phi_{z_t}\right)\exp\left(j\phi_{cons,t}\right)\\ &\times\mathrm{sinc}\left[B\left(t-\frac{2R_t}{c}\right)\right]\mathrm{sinc}\left\{T_a\left(1-\frac{\left(n-1\right)d}{2V_aT_a}\right)\left[f_a+\left(1-\frac{z_t^2-2Hz_t}{2R_t^2}\right)\left(\frac{2v_r}{\lambda}-\frac{2V_a}{\lambda}\cos\theta_{cone,t}+\frac{2d_{pc\_n}\left(V_a-v_y\right)}{\lambda R_t}\right)\right]\right\}\end{aligned} \quad (20)$$

where $\phi_{cons,t}=-\frac{4\pi}{\lambda}R_t+\frac{4\pi}{\lambda}\left(1-\frac{z_t^2-2Hz_t}{2R_t^2}\right)\frac{N-1}{4}d\cos\theta_{cone,t}$.

position, and terrain altitude.

When z_c=0, (25) can be rewritten in (26) below.

From the first and third terms of (26), one can see that the existences of B_x and B_z lead to the severe range-dependence of clutter, deteriorating the clutter suppression performance and AMTI ability.

Note that the interference phase in (25) includes both flat and terrain interference phases, and the interference phase in (26) describes the flat interference phase introduced by CTB. Then, the terrain interference phase caused by the CTB and terrain fluctuation can be computed in (27) shown in the next page.

Based on the above analysis, one can see that the existence of CTB makes the clutter exhibit the range-dependence and topography-dependence, significantly degrading the clutter suppression performance since the i.i.d. property of range training samples is destroyed.

D. Multi-channel Clutter Suppression and Moving Target Detection

According to (20) and (21), for a moving target located at the cone angle of $\theta_{cone,t}$, its Doppler frequency can be expressed as

$$f_{a0} = -\left(1-\frac{z_t^2-2Hz_t}{2R_t^2}\right)\frac{2}{\lambda}\left(v_r - V_a\cos\theta_{cone,t}\right) \tag{28}$$

From (28), one can see that, due to the radial velocity of an AMT, the target is shifted to the Doppler position of f_{a0}, indicating that this target is buried within the clutter at the same Doppler gate but with different cone angles.

According to (20), (21) and (28), the spatial steering vector of a moving target can be expressed in (29) shown in the next page.

It can be seen from (29) that, the spatial baselines of this DSBR system are non-uniform due to the existence of long distance between two satellites, causing a large number of grating lobes in the main lobe clutter regions. In addition, the target blind velocities appear caused by the sparsely

$$\begin{aligned} s_{sr,2,n}(t,f_a) \approx{}& \left(1-\frac{(n-1)d+B_y}{2V_aT_a}\right)G_{azi}\sigma_{s,2}\,\mathrm{sinc}\left[B\left(t-\frac{2R_t}{c}\right)\right]\exp\left(j\phi_{z_t}\right)\exp\left(j\phi_{cons,t}\right)\exp\left(j\phi_{CTB,t}\right)\\ &\times\exp\left\{-j\frac{\pi}{\lambda}\left(1-\frac{z_t^2-2Hz_t}{2R_t^2}\right)\frac{\left[(n-1)d+B_y\right]B_xv_x}{V_aR_t}\right\}\exp\left\{j\frac{2\pi}{\lambda}\left(1-\frac{z_t^2-2Hz_t}{2R_t^2}\right)\left[(n-1)d+B_y\right]\cos\theta_{cone,t}\right\}\\ &\times\mathrm{sinc}\left\{T_a\left(1-\frac{(n-1)d+B_y}{2V_aT_a}\right)\left[f_a+\left(1-\frac{z_t^2-2Hz_t}{2R_t^2}\right)\left(\frac{2v_r}{\lambda}-\frac{2V_a}{\lambda}\cos\theta_{cone,t}+\frac{2d_{pc\_n}\left(V_a-v_y\right)}{\lambda R_t}+\frac{B_y\left(V_a-v_y\right)}{\lambda R_t}-\frac{B_xv_x}{\lambda R_t}\right)\right]\right\} \end{aligned} \tag{21}$$

where G_{azi} denotes the azimuth FFT gain.

$$\begin{aligned} s_{cr,1,n}(t,f_a) \approx{}& \left(1-\frac{(n-1)d}{2V_aT_a}\right)G_{azi}\sigma_{c,1}\exp\left\{j\frac{2\pi}{\lambda}\left(1-\frac{z_c^2-2Hz_c}{2R_c^2}\right)(n-1)d\cos\theta_{cone,c}\right\}\exp\left(j\phi_{z_c}\right)\exp\left(j\phi_{cons,c}\right)\\ &\times\mathrm{sinc}\left[B\left(t-\frac{2R_c}{c}\right)\right]\mathrm{sinc}\left\{T_a\left(1-\frac{(n-1)d}{2V_aT_a}\right)\left[f_a+\left(1-\frac{z_c^2-2Hz_c}{2R_c^2}\right)\left(-\frac{2V_a}{\lambda}\cos\theta_{cone,c}+\frac{2d_{pc\_n}V_a}{\lambda R_c}\right)\right]\right\} \end{aligned} \tag{22}$$

where $\phi_{cons,c} = -\frac{4\pi}{\lambda}R_c + \frac{4\pi}{\lambda}\left(1-\frac{z_c^2-2Hz_c}{2R_c^2}\right)\frac{N-1}{4}d\cos\theta_{cone,c}$.

$$\begin{aligned} s_{cr,2,n}(t,f_a) \approx{}& \left(1-\frac{(n-1)d+B_y}{2V_aT_a}\right)G_{azi}\sigma_{c,2}\,\mathrm{sinc}\left[B\left(t-\frac{2R_c}{c}\right)\right]\exp\left(j\phi_{z_c}\right)\exp\left(j\phi_{cons,c}\right)\exp\left(j\phi_{CTB,c}\right)\\ &\times\exp\left\{j\frac{2\pi}{\lambda}\left(1-\frac{z_c^2-2Hz_c}{2R_c^2}\right)\left[(n-1)d+B_y\right]\cos\theta_{cone,c}\right\}\\ &\times\mathrm{sinc}\left\{T_a\left(1-\frac{(n-1)d+B_y}{2V_aT_a}\right)\left[f_a+\left(1-\frac{z_c^2-2Hz_c}{2R_c^2}\right)\left(-\frac{2V_a}{\lambda}\cos\theta_{cone,c}+\frac{2d_{pc\_n}V_a}{\lambda R_c}+\frac{B_yV_a}{\lambda R_c}\right)\right]\right\} \end{aligned} \tag{23}$$

$$\begin{aligned} \phi_0\big|_{z_c=0} &\approx -\frac{2\pi}{\lambda}\left(-\frac{B_xx_c}{R_c}-\frac{B_yy_c}{R_c}+\frac{B_zH}{R_c}\right)\\ &= \frac{2\pi}{\lambda}\cdot B_x\sqrt{\sin^2\theta_{EL,c}-\left(\frac{\lambda f_{a0}}{2V_a}\right)^2}+\frac{\pi}{\lambda}\cdot B_y\cdot\frac{\lambda f_{a0}}{V_a}-\frac{2\pi}{\lambda}\cdot B_z\cos\theta_{EL,c} \end{aligned} \tag{26}$$

where $f_{a0}=\frac{2}{\lambda}V_a\cos\theta_{cone,c}$.

distributed receiver phase centers. Besides, due to the existence of CTB along *X-axis* and *Z-axis*, the spatial steering vector exhibits the range-dependence and topography-dependence.

Suppose that the cone angle of the clutter component is $\theta_{cone,c}$. According to (22) and (23), the clutter Doppler frequency can be expressed as

$$f_{a0} = \left(1 - \frac{z_c^2 - 2Hz_c}{2R_c^2}\right)\frac{2}{\lambda}V_a \cos\theta_{cone,c} \tag{30}$$

According to (22), (23) and (30), the spatial steering vector of the clutter scatter located at the cone angle of $\theta_{cone,c}$ can be obtained in (31) below.

For a given range gate r_i and a Doppler frequency f_{a0}, the target and clutter returns are arranged along the spatial channels, and then the multi-channel signal vectors can be expressed as a binary detection hypothesis, i.e.,

$$\begin{aligned} H_0 &: \boldsymbol{x}(r_i, f_{a0}) = \boldsymbol{c}(r_i, f_{a0}) + \boldsymbol{n} \\ &= \boldsymbol{\Gamma}(r_i, f_{a0})\boldsymbol{\gamma}_c(r_i, f_{a0})\boldsymbol{a}_{s,c}\left(f_{a0}\right) + \boldsymbol{n} \\ H_1 &: \boldsymbol{x}(r_i, f_{a0}) = \boldsymbol{s}(r_i, f_{a0}) + \boldsymbol{c}(r_i, f_{a0}) + \boldsymbol{n} \\ &= \boldsymbol{\Gamma}(r_i, f_{a0})\begin{bmatrix}\boldsymbol{\gamma}_c(r_i, f_{a0})\boldsymbol{a}_{s,c}\left(f_{a0}\right) \\ +\boldsymbol{\gamma}_s(r_i, f_{a0})\boldsymbol{a}_{s,s}\left(f_{a0}\right)\end{bmatrix} + \boldsymbol{n} \end{aligned} \tag{32}$$

where H_0 denotes that the detection cell without targets, and H_1 denotes that the detection cell with targets. $\boldsymbol{s}$, $\boldsymbol{c}$ and $\boldsymbol{n}$ represent target echo signal, clutter echo signal, and additive white Gaussian noise, respectively. $\boldsymbol{\Gamma}(r_i, f_{a0}) = diag\left\{\zeta_1 e^{j\psi_{error,1}} \quad \zeta_2 e^{j\psi_{error,2}} \quad \cdots \quad \zeta_{2N} e^{j\psi_{error,2N}}\right\}$ represents the interchannel amplitude and phase errors caused by various non-ideal factors, where $\{\zeta_m\}_{m=2}^{2N}$ denote the interchannel amplitude errors and $\{\psi_{error,m}\}_{m=2}^{2N}$ denote the interchannel phase errors. $\gamma_{c1} = G_{azi}\sigma_{c,1}$ and $\gamma_{c2} = G_{azi}\sigma_{c,2}$ represent, respectively, the clutter amplitudes of the main and auxiliary satellites. $\gamma_{s1} = G_{azi}\sigma_{s,1}$ and $\gamma_{s2} = G_{azi}\sigma_{s,2}$ represent the target amplitudes of the main and auxiliary satellites, respectively. $\boldsymbol{\gamma}_c(r_i, f_{a0}) = diag\{\gamma_{c1}, \gamma_{c2}\} \otimes \boldsymbol{I}_N$ and $\boldsymbol{\gamma}_s(r_i, f_{a0}) = diag\{\gamma_{s1}, \gamma_{s2}\} \otimes \boldsymbol{I}_N$, where " $\otimes$ " represents Kronecker product. $\boldsymbol{I}_N$ represents the $N \times N$ identity matrix.

Then, the multi-channel clutter suppression and moving target detection in the post-Doppler domain can be realized by solving the following optimization problem [18], i.e.,

$$\begin{cases} \min\limits_{\boldsymbol{W}} & \boldsymbol{W}^H \boldsymbol{R}_{cn} \boldsymbol{W} \\ s.t. & \boldsymbol{W}^H \boldsymbol{a}_{s,s} = 1 \end{cases} \tag{33}$$

where $\boldsymbol{R}_{cn}$ represents the correlation matrix of clutter plus noise.

According to the linear constraint minimum variance criterion, the optimal solution of (33) can be calculated as [18]

$$\boldsymbol{W}_{opt} = \frac{\boldsymbol{R}_{cn}^{-1}\boldsymbol{a}_{s,s}}{\boldsymbol{a}_{s,s}^H \boldsymbol{R}_{cn}^{-1}\boldsymbol{a}_{s,s}} \tag{34}$$

Assuming that clutter returns is uncorrelated with noise, according to (32), $\boldsymbol{R}_{cn}$ is usually obtained by using the maximum likelihood estimation of the adjacent L range samples, i.e.,

---

$$\begin{aligned} \phi_h &= \phi\big|_{z_c \neq 0} - \phi_0\big|_{z_c = 0} \\ &\approx 2\pi \cdot \frac{z_c^2 - 2Hz_c}{2R_c^2}\left(-\frac{B_x}{\lambda}\sqrt{\sin^2\theta_{EL,c} - 4f_{a0\_c}^2} - \frac{2B_y}{\lambda}f_{a0\_c} + \frac{B_z\cos\theta_{EL,c}}{\lambda} - \frac{B_z z_c}{\lambda R_c}\right) + 2\pi\frac{B_z z_c}{\lambda R_c} \end{aligned} \tag{27}$$

where $f_{a0\_c} = \frac{\lambda}{4V_a} \cdot \frac{f_{a0}}{\left(1 - \frac{z_c^2 - 2Hz_c}{2R_c^2}\right)}$.

$$\begin{aligned} \boldsymbol{a}_{s,s}\left(f_{a0}\right) &= \exp\left\{j\pi\frac{\boldsymbol{d}_{baseline}}{V_a}\left[f_{a0} + \left(1 - \frac{z_t^2 - 2Hz_t}{2R_t^2}\right)\frac{2v_r}{\lambda}\right]\right\} \\ &\odot \exp\left\{j\frac{2\pi}{\lambda}\left(1 - \frac{z_t^2 - 2Hz_t}{2R_t^2}\right)\left[B_x\sqrt{\sin\theta_{EL,t}^2 - f_{a0\_t}^2} - B_z\cos\theta_{EL,t} + B_z z_t\right]\begin{bmatrix}\boldsymbol{O}_{N\times 1} \\ \boldsymbol{Q}_{N\times 1}\end{bmatrix}\right\} \end{aligned} \tag{29}$$

where $\boldsymbol{d}_{baseline} = \begin{bmatrix}0 & d & \cdots & (N-1)d & B_y & B_y + d & \cdots & B_y + (N-1)d\end{bmatrix}^T$ represents the ATB and $f_{a0\_t} = \frac{\lambda}{4V_a}\left[\frac{f_{a0}}{\left(1 - \frac{z_t^2 - 2Hz_t}{2R_t^2}\right)} + \frac{2v_r}{\lambda}\right]$. $\boldsymbol{O}_{N\times 1}$ denotes the all 0 vector of $N \times 1$, $\boldsymbol{Q}_{N\times 1}$ denotes the all 1 vector of $N \times 1$, and " $\odot$ " represents the matrix inner product.

$$\boldsymbol{a}_{s,c}\left(f_{a0}\right) = \exp\left\{j\pi\frac{\boldsymbol{d}_{baseline}}{V_a}f_{a0}\right\} \odot \exp\left\{j\frac{2\pi}{\lambda}\left(1 - \frac{z_c^2 - 2Hz_c}{2R_c^2}\right)\left(B_x\sqrt{\sin^2\theta_{EL,c} - f_{a0\_c}^2} - B_z\cos\theta_{EL,c} + B_z z_c\right)\begin{bmatrix}\boldsymbol{O}_{N\times 1} \\ \boldsymbol{Q}_{N\times 1}\end{bmatrix}\right\} \tag{31}$$

$$\begin{aligned}\boldsymbol{R}_{cn} &= \frac{1}{L}\sum_{i=1}^{L}\boldsymbol{x}(r_i, f_{a0})\boldsymbol{x}^H(r_i, f_{a0}) \\ &= \boldsymbol{R}_c + \sigma_n^2\boldsymbol{I}_{2N} \\ &= \left(\begin{bmatrix}\gamma_{c1}\\ \gamma_{c2}\end{bmatrix}\otimes\boldsymbol{Q}_{N\times 1}\odot\boldsymbol{a}_{s,c}\right)\left(\begin{bmatrix}\gamma_{c1}\\ \gamma_{c2}\end{bmatrix}\otimes\boldsymbol{Q}_{N\times 1}\odot\boldsymbol{a}_{s,c}\right)^H\odot\boldsymbol{\rho}+\sigma_n^2\boldsymbol{I}_{2N}\end{aligned} \tag{35}$$

where $\boldsymbol{R}_c$ represents the clutter correlation matrix, and σ_n^2 represents the noise power. $\boldsymbol{\rho}=\begin{bmatrix}1 & \rho_{1,2} & \cdots & \rho_{1,2N}\\ \rho_{1,2}^* & 1 & \cdots & \rho_{2,2N}\\ \vdots & \vdots & \cdots & \vdots\\ \rho_{1,2N}^* & \rho_{2,2N}^* & \cdots & 1\end{bmatrix}$ represents the clutter correlation coefficient matrix, where $\rho_{m,n}$ denotes the clutter correlation coefficient between the *n*th spatial channel and the *m*th, $m,n=1,2,...,2N$, spatial channel at the Doppler frequency f_{a0}, i.e.,

$$\rho_{m,n}=\frac{\sum_{i=1}^{L}x_m(r_i, f_{a0})x_n^*(r_i, f_{a0})}{\sqrt{\left(\sum_{i=1}^{L}x_m(r_i, f_{a0})x_m^*(r_i, f_{a0})\right)\left(\sum_{i=1}^{L}x_n(r_i, f_{a0})x_n^*(r_i, f_{a0})\right)}} \tag{36}$$

where x_m and x_n denote the complex echo data of the *m*th spatial channel and the *n*th spatial channel, respectively. "*" denotes the complex conjugate operation.

Considering that the clutter correlation matrix is a Hermite matrix, after performing the eigen decomposition, one has

$$\begin{aligned}\boldsymbol{R}_{cn} &= \boldsymbol{R}_c + \sigma_n^2\boldsymbol{I}_{2N} \\ &= \sum_{i=1}^{p}\lambda_i\boldsymbol{v}_i\boldsymbol{v}_i^H + \sigma_n^2\sum_{i=p+1}^{2N}\boldsymbol{v}_i\boldsymbol{v}_i^H\end{aligned} \tag{37}$$

where $\lambda_1\ge\lambda_2\ge\cdots\ge\lambda_p$ denote the *p* largest eigenvalues of the covariance matrix $\boldsymbol{R}_{cn}$. Note that *p*=1 usually holds if range ambiguity and Doppler ambiguity do not exist. The eigenvectors corresponding to the p largest eigenvalues form the clutter subspace, i.e., $\Theta_c = span\{\boldsymbol{v}_1, \boldsymbol{v}_2, \cdots, \boldsymbol{v}_p\}$, with the clutter DOF being *p*.

Ideally, the clutter signals in different spatial channels are highly correlated and the clutter DOF (the number of large eigenvalues obtained from the eigen decomposition of clutter correlation matrix) is 1. However, in fact, due to the existence of many non-ideal factors, such as interferometric phase caused by the relatively large CTB between different satellites, terrain fluctuation, interchannel amplitude and phase errors, and synchronization errors, the correlation between different spatial channels decreases and the clutter DOF increases, which causes the clutter expanding along the space and time dimensions, degrading the subsequent clutter rejection performance and widening the clutter filtering notch.

III. Influencing Factor Analysis for AMTI in a DSBR System

In the following, we will analytically study the above mentioned nonideal factors one by one (see Section II). We first see how the channel noise affects the echo correlation.

A. Influence of Channel Noise on Echo Correlation

In order to analyze the only influence of channel noise on echo correlation, the various non-ideal factors and the factors from the spatial baselines are not taken into account. The received echo signal in a spatial channel contains two parts: clutter/target echo signal which is correlated between different channels and channel noise which is uncorrelated between different channels. Obviously, the interchannel-uncorrelated part will deteriorate the echo correlation between different channels. Assuming that the azimuth antennas of the main and auxiliary satellites are uniformly divided into *N* equivalent channels, the echo signal of the same clutter scattering unit in the *n*th channel can be expressed as

$$s_{cr,n} = c_{cr,n} + n_n \tag{38}$$

where $c_{cr,n}$ and n_n represent the clutter component and noise component of the *n*th channel, respectively. It is noted that the noise components of different channels are uncorrelated. Considering that the azimuth antennas of main and auxiliary satellites are uniformly divided, the clutter amplitudes of different channels are the same, i.e., $|c_{cr,1}|=|c_{cr,2}|=\cdots=|c_{cr,N}|=\gamma_{c1}$, $|c_{cr,N+1}|=|c_{cr,N+2}|=\cdots=|c_{cr,2N}|=\gamma_{c2}$.

The correlation coefficient between the *n*th channel and the *m*th channel can be expressed in (39) below [56].

Considering that the noise components are uncorrelated, one has, $E\left(n_m\cdot n_n^*\right)=0$. Then (39) can be further simplified as

$$\begin{aligned}\rho_{CNR\_m,n} &= \frac{E\left[s_{cr,m}s_{cr,n}^*\right]}{\sqrt{E\left[s_{cr,m}s_{cr,m}^*\right]E\left[s_{cr,n}s_{cr,n}^*\right]}} \\ &= \frac{E\left[\left(c_{cr,m}+n_m\right)\left(c_{cr,n}+n_n\right)^*\right]}{\sqrt{E\left[\left(c_{cr,m}+n_m\right)\left(c_{cr,m}+n_m\right)^*\right]E\left[\left(c_{cr,n}+n_n\right)\left(c_{cr,n}+n_n\right)^*\right]}} \\ &= \frac{E\left(c_{cr,m}\cdot c_{cr,n}^*\right)+E\left(c_{cr,m}\cdot n_n^*\right)+E\left(n_m\cdot c_{cr,n}^*\right)+E\left(n_m\cdot n_n^*\right)}{\sqrt{\begin{array}{l}\left[E\left(c_{cr,m}\cdot c_{cr,m}^*\right)+E\left(c_{cr,m}\cdot n_m^*\right)+E\left(n_m\cdot c_{cr,\mathrm{m}}^*\right)+E\left(n_m\cdot n_m^*\right)\right]\\ \times\left[E\left(c_{cr,n}\cdot c_{cr,\mathrm{n}}^*\right)+E\left(c_{cr,n}\cdot n_n^*\right)+E\left(n_n\cdot c_{cr,n}^*\right)+E\left(n_n\cdot n_n^*\right)\right]\end{array}}}\end{aligned} \tag{39}$$

$$\begin{aligned}\rho_{CNR\_m,n} &= \frac{E\left(c_{cr,m}\cdot c_{cr,n}^{*}\right)}{\sqrt{\left[E\left(c_{cr,m}\cdot c_{cr,m}^{*}\right)+E\left(n_m\cdot n_m^{*}\right)\right]\times\left[E\left(c_{cr,n}\cdot c_{cr,\mathrm{n}}^{*}\right)+E\left(n_n\cdot n_n^{*}\right)\right]}} \\ &= \frac{\left|c_{cr,m}\right|\left|c_{cr,n}\right|}{\sqrt{\left(\left|c_{cr,m}\right|^2+\sigma_n^2\right)\left(\left|c_{cr,n}\right|^2+\sigma_n^2\right)}} \\ &= \frac{\sqrt{CNR_m CNR_n}}{\sqrt{\left(CNR_m+1\right)\left(CNR_n+1\right)}} \\ &= \frac{1}{\sqrt{\left(1+CNR_m^{-1}\right)\left(1+CNR_n^{-1}\right)}}\end{aligned} \tag{40}$$

where CNR_m and CNR_n represent the clutter to noise ratios (CNRs) of the mth channel and the nth channel, respectively. Obviously, the interchannel correlation coefficient is smaller than 1.

Without considering the influences of other actual factors, the correlation coefficient matrix can be expressed in (41) below.

B. Influence of ATB on Echo Correlation

From (16) and (17), it can be seen that, due to the location differences of receiving channels, the slow-time spectrums of echo returns shift, introducing the azimuth registration error caused by B_y after implementing the Doppler localization.

By comparing (22) and (23), one can see that the Doppler offset, $z_c = 0$, between the echo data of main satellite and auxiliary satellite can be calculated as

$$\Delta f_a = \left| f_{dc1} - f_{dc2} \right| = \frac{B_y V_a}{\lambda R_c} \tag{42}$$

where f_{dc1} and f_{dc2} denote, respectively, the clutter Doppler center frequencies of the main and auxiliary satellites.

It is observed from (42) that after Doppler localization, the azimuth registration error is $B_y/2$ m. In order to maintain the formation pattern of the DSBR system and prevent satellite collisions, the reasonable ATB length between the main and auxiliary satellites is usually chosen as 150~200 m [57][58].

From Fig. 2(a), it is apparent that when the ATB reaches 200 m, according to the system parameters listed in Table I, the azimuth registration error is up to be half a Doppler resolution unit. Fig. 2(b) shows the relationship between the interchannel correlation coefficient and the azimuth registration error, from which it is clearly seen that, the larger the azimuth registration error, the lower the interchannel correlation coefficient, thus drastically degrading the STAP performance. Obviously, for a DSBR system with intersatellite ATB of 200m, the correlation coefficient of the radar returns of the main satellite and auxiliary satellite drops to 0.62, causing the multi-channel clutter suppression ability of STAP to decrease dramatically. Therefore, the accurate azimuth registration error compensation is required in order to improve the subsequent STAP ability in a DSBR system.

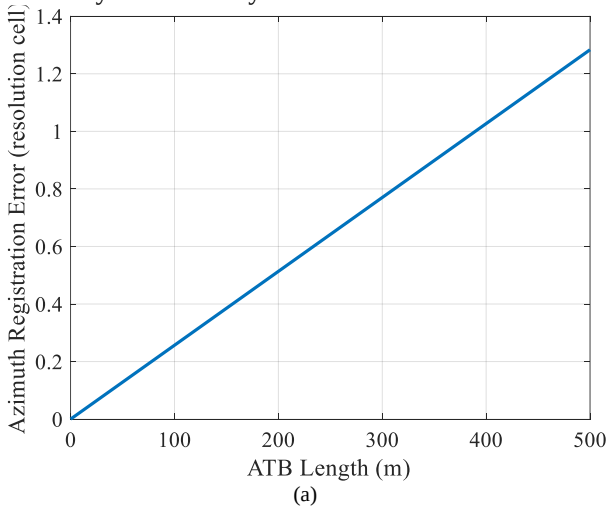

(a)

$$\begin{aligned}\boldsymbol{\rho}_{CNR} &= \begin{bmatrix} \rho_{CNR\_1,1} & \cdots & \rho_{CNR\_1,N} & \rho_{CNR\_1,N+1} & \cdots & \rho_{CNR\_1,2N} \\ \vdots & \ddots & \vdots & \vdots & \ddots & \vdots \\ \rho_{CNR\_1,N}^{*} & \cdots & \rho_{CNR\_N,N} & \rho_{CNR\_N,N+1} & \cdots & \rho_{CNR\_N,2N} \\ \rho_{CNR\_1,N+1}^{*} & \cdots & \rho_{CNR\_N,N+1}^{*} & \rho_{CNR\_N+1,N+1} & \cdots & \rho_{CNR\_N+1,2N} \\ \vdots & \ddots & \vdots & \vdots & \ddots & \vdots \\ \rho_{CNR\_1,2N}^{*} & \cdots & \rho_{CNR\_N,2N}^{*} & \rho_{CNR\_N+1,2N}^{*} & \cdots & \rho_{CNR\_2N,2N} \end{bmatrix} \\ &= \begin{bmatrix} \dfrac{1}{1+CNR_{main}^{-1}} & \dfrac{1}{\sqrt{\left(1+CNR_{main}^{-1}\right)\left(1+CNR_{auxi}^{-1}\right)}} \\ \dfrac{1}{\sqrt{\left(1+CNR_{main}^{-1}\right)\left(1+CNR_{auxi}^{-1}\right)}} & \dfrac{1}{1+CNR_{auxi}^{-1}} \end{bmatrix} \otimes \boldsymbol{Q}_{N\times 1}\boldsymbol{Q}_{N\times 1}^{T}\end{aligned} \tag{41}$$

where CNR_{main} and CNR_{auxi} represent the CNRs of a received channel data associated with the main and auxiliary satellites, respectively.

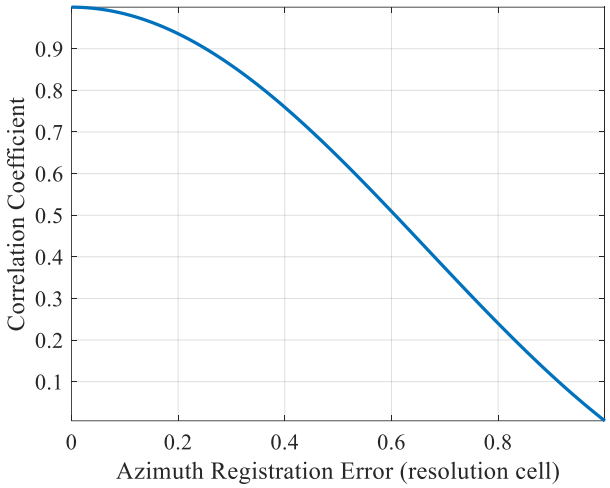

(b)

Fig. 2 Influence of the azimuth registration error. (a) Relationships between azimuth registration error and ATB length. (b) Relationships between correlation coefficient and azimuth registration error.

In practice, the *prior* information of ATB can be used for azimuth registration. However, due to the actual baseline measurement error, the residual registration errors inevitably exist, reducing the echo correlation corresponding to different spatial channels. Assuming that the baseline measurement error of the DSBR system is ΔB_y, then after performing the preliminary registration by using the *prior* radar system information, the residual azimuth registration error is $\Delta B_y V_a T_a / \lambda R_0$.

In addition, due to the difference between the slow-time window of the radar return in the auxiliary satellite and the slow-time window of the quadratic phase compensation function shown in (11), the existence of ATB will cause the energy loss of azimuth coherent integration. The energy loss of azimuth coherent integration can be calculated as (this energy loss can be contributed to the interchannel amplitude error)

$$G_{azi\_loss} = 10\log\left(1 - \frac{\Delta B_y V_a}{\lambda R_0} \Big/ B_d\right) \text{ in dB} \tag{43}$$

where B_d represents the clutter Doppler bandwidth.

Fig. 3 and Table I exhibit the relationship between the energy loss of azimuth coherent integration and the ATB length, from which it is clear that, the energy loss is more and more severe with the increasing of ATB length.

TABLE I
AZIMUTH COMPRESSION LOSS VERSUS WITH ATB LENGTH

ATB length (m)	100	200	300	400	500
Azimuth compression loss (dB)	0.025	0.049	0.074	0.099	0.124

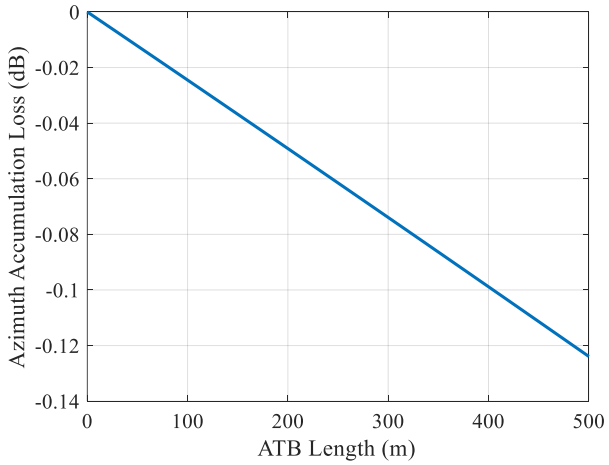

Fig. 3 Relationship between the azimuth compression loss and ATB length.

C. Influence of CTB on Echo Correlation

Proverbially, the pure along-track alignment of multi-channel phase centers is the optimal configuration for AMTI. However, as mentioned in Introduction, in addition to have AMTI, spaceborne radars may need to have InSAR function. Thus, both ATB and CTB between two satellites are used. Unfortunately, the existence of CTB leads to the elevation angle deviation between the main and auxiliary satellites, which will cause the scattering characteristics distribution of ground points randomly varying along range dimension, decreasing the channel correlation.

Suppose that a linear frequency modulated (LFM) signal in (1) is adopted as the radar waveform transmitted by the main satellite. For convenience, only the range-dimensional echo signals are considered in the following analysis. Taking the position of the nadir point with respect to the main satellite as the coordinate axis origin, then the echo signal corresponding to a scattering point on the ground in the main and auxiliary satellites can be expressed as

$$\begin{aligned} s_{R,i}(t;r_t) = \gamma(r_t)\, rect\left(\frac{t-\tau_i}{T_P}\right)\exp\left\{j\pi K(t-\tau_i)^2\right\} \\ \times\exp\left\{j2\pi f_0(t-\tau_i)\right\} \end{aligned} \tag{44}$$

where $\tau_1 \approx 2\left[R_{0,1} - (r_t - r_{0,1})\sin\theta_{EL1}\right]/c$ represents the two-way propagation delay between this scattering point and the main satellite and $\tau_2 \approx 2\left[R_{0,2} - (r_t - r_{0,1})\sin\theta_{EL2}\right]/c$ represents the two-way propagation delay between this scattering point and the auxiliary satellite. $R_{0,1}$ and $R_{0,2}$ represent the slant-distances of the beam center relative to the main and auxiliary satellites, respectively. r_t denotes the ground projection of the slant-distance of the scattering point relative to the main satellite along range dimension. $r_{0,1}$ denotes the ground distance of the beam center with respect to the main satellite. θ_{EL1} and θ_{EL2} denote, respectively, the elevation angles of the scattering point relative to the main and auxiliary satellites.

After range compression and down modulation, the baseband echo signals of the main and auxiliary satellites can be, respectively, expressed as

$$s_{R,1}(t;r_u)=\gamma(r_u)\,\mathrm{sinc}\left[B\left(t-\frac{2R_{0,1}-2r_u\sin\theta_{EL1}}{c}\right)\right]\times\exp\left(-j4\pi f_0\frac{R_{0,1}}{c}\right)\exp\left(j4\pi f_0\frac{r_u\sin\theta_{EL1}}{c}\right) \tag{45}$$

$$s_{R,2}(t;r_u)=\gamma(r_u)\,\mathrm{sinc}\left[B\left(t-\frac{2R_{0,2}-2r_u\sin\theta_{EL2}}{c}\right)\right]\times\exp\left(-j4\pi f_0\frac{R_{0,2}}{c}\right)\exp\left(j4\pi f_0\frac{r_u\sin\theta_{EL2}}{c}\right) \tag{46}$$

where $r_u=r_t-r_{0,1}$.

After performing the FFT on (45) and (46) along range dimension, the echo signals in the wavenumber domain can be, respectively, noted as

$$s_{R,1}(t;k_r)\approx\Gamma\left(k_r-\frac{4\pi f_0\sin\theta_{EL1}}{c}\right)\exp\left(-j4\pi f_0\frac{R_{0,1}}{c}\right)\otimes\left\{rect\left(\frac{c}{4\pi B\sin\theta_{EL1}}k_r\right)\times\exp\left[-j\frac{ck_r}{2\sin\theta_{EL1}}\left(t-\frac{2R_{0,1}}{c}\right)\right]\right\} \tag{47}$$

$$s_{R,2}(t;k_r)\approx\Gamma\left(k_r-\frac{4\pi f_0\sin\theta_{EL2}}{c}\right)\exp\left(-j4\pi f_0\frac{R_{0,2}}{c}\right)\otimes\left\{rect\left(\frac{c}{4\pi B\sin\theta_{EL2}}k_r\right)\times\exp\left[-j\frac{ck_r}{2\sin\theta_{EL2}}\left(t-\frac{2R_{0,2}}{c}\right)\right]\right\} \tag{48}$$

where $k_r=4\pi f\sin\theta_{EL1}/c$, $f\in[f_0-B/2,\,f_0+B/2]$, represents the wavenumber variable.

It can be seen that the wavenumber spectrums of the echo signals in the main and auxiliary satellites exhibit a relative offset, which can be calculated as

$$\Delta k_r=\left|\frac{4\pi f_0}{c}\left(\sin\theta_{EL2}-\sin\theta_{EL1}\right)\right| \tag{49}$$

The echo correlation coefficient can be expressed as

$$\rho_{ct}\approx 1-\left|\frac{4\pi f_0\left(\sin\theta_{EL2}-\sin\theta_{EL1}\right)/c}{4\pi B\sin\theta_{EL1}/c}\right|=1-\left|\frac{f_0}{B}\left(\frac{\sin\theta_{EL2}}{\sin\theta_{EL1}}-1\right)\right| \tag{50}$$

According to the geometry in Fig. 1, (49) can be further expressed as

$$\rho_{ct}=1-\left|\frac{f_0}{B}\left[1-\frac{\sin\left(\arctan\left(\frac{H\tan\theta_{EL1}+B_x}{H+B_z}\right)\right)}{\sin\theta_{EL1}}\right]\right| \tag{51}$$

D. Influences of Interchannel Amplitude and Phase Errors on Echo Correlation

For the whole antenna array, due to space environmental conditions, service life, engineering processing, and other factors [63], the simulators may be inconsistent in different spatial channels, which may cause the inconsistency of amplitudes and phases among different receiving channels, introducing the interchannel amplitude and phase errors. In addition, it can be seen from (20), (21), (22) and (23) that the channel position differences lead to the energy loss after implementing the coherent accumulation, which also causes the interchannel amplitude error.

In order to analyze the influence of interchannel amplitude and phase errors on channel correlation, other non-ideal factors are not taken into account. The steering vector is supposed as $[1,...,1]_{N\times1}^T$. Then, according to (32), the echo x_m of the *m*th channel can be expressed as

$$x_m=\zeta_m e^{j\psi_{error,m}}\gamma_{c1} \tag{52}$$

where the symbols $\mu_m=\zeta_m-1$ and $\psi_{error,m}$ follow Gaussian distributions with mean 0 and variances σ_ζ^2 and σ_ϕ^2, respectively. Obviously, the channel correlation coefficient between the echoes of the *m*th channel and that of the first channel is

$$\rho_m=\frac{E\left[x_1x_m^*\right]}{\sqrt{E\left[x_1x_1^*\right]E\left[x_mx_m^*\right]}}=\frac{E\left[\zeta_m e^{-j\psi_{error,m}}\right]}{\sqrt{E\left[\zeta_m^2\right]}}=\frac{E[\zeta_m]E\left[e^{-j\psi_{error,m}}\right]}{\sqrt{E\left[\zeta_m^2\right]}}=e^{-\frac{\sigma_\phi^2}{2}}\Big/\sqrt{1+\sigma_\zeta^2} \tag{53}$$

where

$$\begin{aligned}E\left[\zeta_m^2\right]&=E\left[(\mu_m+1)^2\right]\\&=E\left[\mu_m^2\right]+2E\left[\mu_m\right]+E[1]\\&=E[1]+\sigma_\zeta^2\\&=1+\sigma_\zeta^2\end{aligned} \tag{54}$$

$$E\left[e^{-j\psi_{error,m}}\right]=\int_{-\infty}^{\infty}e^{-j\psi_{error,m}}\frac{1}{\sigma_\phi\sqrt{2\pi}}\exp\left\{-\frac{\psi_{error,m}^2}{2\sigma_\phi^2}\right\}d\psi_{error,m}=e^{-\frac{\sigma_\phi^2}{2}} \tag{55}$$

E. Influence of Space Synchronization Error on Echo Correlation

For a DSBR system, in order to make the radar returns of two satellites keep the high coherence, two satellite beams must cover the same area. However, if the space synchronization error exists (take the space synchronization error of the auxiliary satellite for example), the beam pointing will rotate and offset. This may cause the elevation angle deviation and squint angle deviation between two satellites, and thus lead to the correlation reduction of the echo data between two satellites.

Fig. 5 gives the space synchronization error model, where *Z-axis* is along the antenna elevation dimension, *Y-axis* is along the antenna azimuth dimension, and *X-axis* is perpendicular to the antenna panel. θ_P, pitch angle, θ_R, roll angle, and θ_Y, yaw angle, represent, respectively, the rotation angles of the antenna panel along *X-axis*, *Y-axis* and *Z-axis*.

Taking the space synchronization error in the auxiliary satellite for example, the influences of yaw angle, pitch angle, and roll angle will be analyzed term by term.

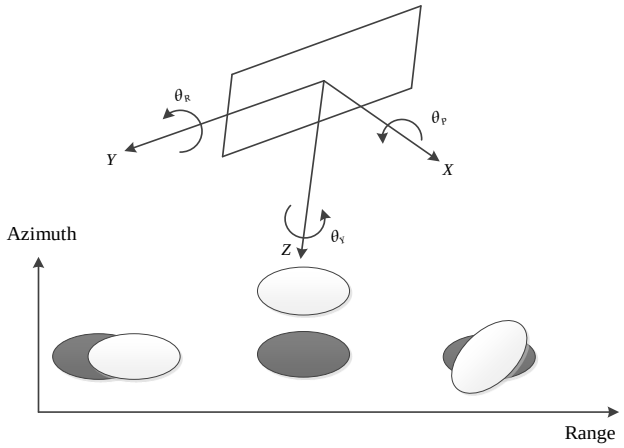

Fig. 4 Space synchronization error model.

1) Influence of yaw angle

In the presence of space synchronization error, the coordinate system of antenna panel (x', y', z') rotates relative to (x, y, z). Assume that the auxiliary satellite adopts the side-looking observation mode without space synchronization errors, the slant-range vector of beam center in (x, y, z) coordinate system under the case of $\theta_{AZ} = \pi/2$ is shown as

$$\vec{\boldsymbol{R}} = \left(R\sin\theta_{EL}, 0, R\cos\theta_{EL}\right)^T \tag{56}$$

In (x', y', z') coordinate system, the satellite slant-range vector is $\vec{\boldsymbol{R}}'$. Assuming that only the influence of yaw angle error is considered, the conversion relation of $\vec{\boldsymbol{R}}$ to $\vec{\boldsymbol{R}}'$ can be expressed as

$$\vec{\boldsymbol{R}}' = \begin{bmatrix} \cos\theta_Y & \sin\theta_Y & 0 \\ -\sin\theta_Y & \cos\theta_Y & 0 \\ 0 & 0 & 1 \end{bmatrix} \begin{bmatrix} R\sin\theta_{EL} \\ 0 \\ R\cos\theta_{EL} \end{bmatrix} = R \begin{bmatrix} \sin\theta_{EL}\cos\theta_Y \\ -\sin\theta_{EL}\sin\theta_Y \\ \cos\theta_{EL} \end{bmatrix} \tag{57}$$

Considering that the satellite attitude error is usually small, $\cos\theta_Y \approx 1$ holds. Then, (57) can be simplified as

$$\vec{\boldsymbol{R}}' \approx R \begin{bmatrix} \sin\theta_{EL} \\ -\sin\theta_{EL}\sin\theta_Y \\ \cos\theta_{EL} \end{bmatrix} \tag{58}$$

From (58), one can see that the yaw angle error leads to an extra squint angle for the beam center, causing the echo Doppler center deviation and the beam coverage area deviation of the auxiliary satellite.

The extra squint angle introduced by yaw angle error can be calculated as

$$\Delta\varphi \approx \arcsin\left(-\sin\theta_Y \sin\theta_{EL}\right) \tag{59}$$

According to (59), Doppler center offset can be calculated as

$$\begin{aligned} \Delta f_{DC\_yaw} &= \frac{2V_a}{\lambda}\sin\left(\varphi + \Delta\varphi\right) - \frac{2V_a}{\lambda}\sin\varphi \\ &\overset{\varphi=0}{=} \frac{2V_a}{\lambda}\sin\Delta\varphi \\ &\approx -\frac{2V_a}{\lambda}\sin\theta_{EL}\sin\theta_Y \end{aligned} \tag{60}$$

In addition, the existence of the yaw angle error will introduce the non-stationarity of the clutter echo received by the auxiliary satellite.

For the ground scattering point *P* located at (x_c, y_c, z_c) (see Fig. 1), the clutter baseband echo signal of the *n*th channel in the auxiliary satellite after range compression and down modulation can be expressed in (61) below.

According to (16) and (61), the spatial steering vector of the clutter located at Doppler unit of f_{a0} can be expressed in (62)

$$\begin{aligned} s_{cr,2,n}(t, t_m; \theta_Y) \approx \sigma_{c,2}\,\mathrm{sinc}\left[B\left(t - \frac{2R_c}{c}\right)\right] rect\left(\frac{t_m + \left(n-1\right)d\cos\theta_Y + B_y \big/ 2V_a}{T_a}\right) rect\left(\frac{t_m}{T_a}\right) \exp\left(j\phi_{z_c}\right)\exp\left(j\phi_{CTB,c}\right) \\ \times\exp\left\{-j\frac{4\pi}{\lambda}\left[R_c - \left(1 - \frac{z_c^2 - 2Hz_c}{2R_c^2}\right)\left(d_{pc\_n}\sin\theta_{EL,c}\cos\left(\theta_{AZ,c} + \theta_Y\right) + \frac{B_y}{2}\cos\theta_{cone,c}\right)\right]\right\} \\ \times\exp\left\{-j\frac{4\pi}{\lambda}\left(1 - \frac{z_c^2 - 2Hz_c}{2R_c^2}\right)\left(-V_a t_m\cos\theta_{cone,c} + \frac{d_{pc\_n}V_a t_m\cos\theta_Y}{R_c} + \frac{B_y V_a t_m}{2R_c}\right)\right\} \end{aligned} \tag{61}$$

$$\begin{aligned} \boldsymbol{a}_{s,c}\left(f_{a0}\right) = \begin{bmatrix} \exp\left(j\pi\dfrac{\boldsymbol{d}_{single}}{V_a}f_{a0}\right) \\ \exp\left[j\pi\dfrac{\boldsymbol{d}_{single}\cos\theta_Y}{V_a}f_{a0}\right] \end{bmatrix} \odot \begin{bmatrix} \boldsymbol{Q}_{N\times 1} \\ \exp\left[-j\dfrac{2\pi}{\lambda}\left(1 - \dfrac{z_c^2 - 2Hz_c}{2R_c^2}\right)\boldsymbol{d}_{single}\sin\theta_Y\sqrt{\sin^2\theta_{EL,c} - f_{a0\_c}^2}\right] \end{bmatrix} \\ \odot\exp\left\{\left[j\pi\frac{B_y}{V_a}f_{a0} + j\frac{2\pi}{\lambda}\left(1 - \frac{z_c^2 - 2Hz_c}{2R_c^2}\right)\left(B_x\sqrt{\sin^2\theta_{EL,c} - f_{a0\_c}^2} - B_z\cos\theta_{EL,c} + B_z z_c\right)\right]\begin{bmatrix}\boldsymbol{O}_{N\times 1} \\ \boldsymbol{Q}_{N\times 1}\end{bmatrix}\right\} \end{aligned} \tag{62}$$

where $\boldsymbol{d}_{single} = \begin{bmatrix}0 & d & \cdots & (N-1)d\end{bmatrix}^T$.

below.

Obviously, the existence of the yaw angle error lead to the non-stationarity of the clutter echo received by the auxiliary satellite, which further damages the i.i.d. property of clutter.

2) Influence of pitch angle

Assuming that only the influence of pitch angle error is considered, then the conversion relation of $\vec{\boldsymbol{R}}$ to $\vec{\boldsymbol{R}}'$ can be expressed as

$$\vec{\boldsymbol{R}}' = \begin{bmatrix} 1 & 0 & 0 \\ 0 & \cos\theta_P & \sin\theta_P \\ 0 & -\sin\theta_P & \cos\theta_P \end{bmatrix} \begin{bmatrix} R\sin\theta_{EL} \\ 0 \\ R\cos\theta_{EL} \end{bmatrix} \approx R \begin{bmatrix} \sin\theta_{EL} \\ \cos\theta_{EL}\sin\theta_P \\ \cos\theta_{EL} \end{bmatrix} \tag{63}$$

Obviously, the influence of pitch angle error is similar to the yaw angle error, which leads to an extra squint angle of the beam center, causing the echo Doppler center deviation and the beam coverage area deviation associated with the auxiliary satellite.

The extra squint angle introduced by yaw angle error can be calculated as

$$\Delta\varphi \approx \arcsin\left(\cos\theta_{EL}\sin\theta_P\right) \tag{64}$$

Then, Doppler center offset can be calculated as

$$\begin{aligned} \Delta f_{DC\_pitch} &= \frac{2V_a}{\lambda}\sin\left(\varphi+\Delta\varphi\right) - \frac{2V_a}{\lambda}\sin\varphi \\ &\overset{\varphi=0}{=} \frac{2V_a}{\lambda}\sin\Delta\varphi \\ &= \frac{2V_a}{\lambda}\cos\theta_{EL}\sin\theta_P \end{aligned} \tag{65}$$

Moreover, the existence of the pitch angle error also introduces the non-stationarity of the clutter echo received by the auxiliary satellite.

With the consideration of the pitch angle error in the clutter echo signal in (17) with respect to the auxiliary satellite, the clutter echo signal of the *n*th channel in the auxiliary satellite after range compression and down modulation can be expressed in (66) below.

According to (16) and (66), the spatial steering vector of the clutter located at Doppler unit of f_{a0} can be expressed in (67) below.

Evidently, the existence of the pitch angle error causes the spatial steering vector of the auxiliary satellite varying along range dimension, also further damaging the i.i.d. property of clutter.

3) Influence of roll angle

Assuming that only the influence of roll angle error is considered, the conversion relation of $\vec{\boldsymbol{R}}$ to $\vec{\boldsymbol{R}}'$ can be expressed as

$$\vec{\boldsymbol{R}}' = \begin{bmatrix} \cos\theta_R & 0 & -\sin\theta_R \\ 0 & 1 & 0 \\ \sin\theta_R & 0 & \cos\theta_R \end{bmatrix} \begin{bmatrix} R\sin\theta_{EL} \\ 0 \\ R\cos\theta_{EL} \end{bmatrix} = \begin{bmatrix} \sin\left(\theta_{EL}-\theta_R\right) \\ 0 \\ \cos\left(\theta_{EL}-\theta_R\right) \end{bmatrix} \tag{68}$$

From (68), one can see that the roll angle error introduces an extra elevation angle, which causes the beam coverage area deviation along range dimension, leading to the deviation of ground scattering spectrum. Thus, according to (68), (49) can be modified as

$$\rho_{ct} = 1 - \left| \frac{f_0}{B}\left(\frac{\sin\left(\theta_{EL2}+\theta_R\right)}{\sin\theta_{EL1}} - 1 \right) \right| \tag{69}$$

F. Influence of Time Synchronization Error on Echo Correlation

In a DSBR system, since the main and auxiliary satellites adopt different frequency bands , the triggering pulses cannot be completely aligned and the actual PRI of the two satellites cannot be strictly equal, resulting in the time synchronization error. In addition, frequency source jitter will also cause time synchronization errors.

The time synchronization error mainly includes two parts [64]: 1) fixed time synchronization error caused by unaligned frequency sources of main and auxiliary satellites; and 2) linear time synchronization error. It can be expressed as

$$e(t_m) = \alpha + \beta t_m \tag{70}$$

$$\begin{aligned} s_{cr,2,n}(t,t_m) \approx \sigma_{c,2}\,\mathrm{sinc}\left[B\left(t-\frac{2R_c}{c}\right)\right] rect\left(\frac{t_m + \left(n-1\right)d\cos\theta_P + B_y \big/ 2V_a}{T_a}\right) rect\left(\frac{t_m}{T_a}\right) \exp\left(j\phi_{z_c}\right)\exp\left(j\phi_{CTB,c}\right) \\ \times\exp\left\{-j\frac{4\pi}{\lambda}\left[R_c - \left(1-\frac{z_c^2-2Hz_c}{2R_c^2}\right)\left(d_{pc\_n}\cos\theta_{cone,c}\cos\theta_P + d_{pc\_n}\cos\theta_{EL,c}\sin\theta_P + \frac{B_y}{2}\cos\theta_{cone,c}\right)\right]\right\} \\ \times\exp\left\{-j\frac{4\pi}{\lambda}\left(1-\frac{z_c^2-2Hz_c}{2R_c^2}\right)\left(-V_a t_m\cos\theta_{cone,c} + \frac{d_{pc\_n}V_a t_m}{R_c} + \frac{B_y V_a t_m}{2R_c}\right)\right\} \end{aligned} \tag{66}$$

$$\begin{aligned} \boldsymbol{a}_{s,c}\left(f_{a0}\right) = \begin{bmatrix} \exp\left(j\pi\dfrac{\boldsymbol{d}_{single}}{V_a}f_{a0}\right) \\ \exp\left[j\pi\dfrac{\boldsymbol{d}_{single}\cos\theta_P}{V_a}f_{a0}\right] \end{bmatrix} \odot \begin{bmatrix} \boldsymbol{Q}_{N\times 1} \\ \exp\left(j2\pi\boldsymbol{d}_{single}\cos\theta_{EL,c}\sin\theta_P\right) \end{bmatrix} \\ \odot\exp\left\{\left[j\pi\frac{B_y}{V_a}f_{a0} + j\frac{2\pi}{\lambda}\left(1-\frac{z_c^2-2Hz_c}{2R_c^2}\right)\left(B_x\sqrt{\sin^2\theta_{EL,c}-f_{a0\_c}^2} - B_z\cos\theta_{EL,c} + B_z z_c\right)\right]\begin{bmatrix}\boldsymbol{O}_{N\times 1} \\ \boldsymbol{Q}_{N\times 1}\end{bmatrix}\right\} \end{aligned} \tag{67}$$

where α represents the fixed time synchronization error, and β represents the linear synchronization error index.

1) Fixed time synchronization error

Assuming that the main satellite transmits linear frequency modulation signals, then the echo signal of the *n*th channel of the auxiliary satellite can be expressed as

$$\begin{aligned} s_{cr,2,n}(t,t_m) = \sigma_{c,2} rect\left(\frac{t_m + \left(n-1\right)d + B_y \big/ 2V_a}{T_a} \right) \\ \times \mathrm{sinc}\left\{ B\left[t - 2R_n\left(t_m\right)/c - \alpha \right] \right\} \\ \times \exp\left(-j2\pi f_0 \alpha\right) \exp\left[-j4\pi f_0 R_n\left(t_m\right)/c \right] \end{aligned} \tag{71}$$

where $\sigma_{c,2}$ represents the signal amplitude after range compression and $R_n\left(t_m\right)$ denotes the two-way instantaneous slant-range between the *n*th spatial received channel of the auxiliary satellite and the ground scatter point.

According to (71), it can be concluded that after range compression, the peak value exhibits the fixed time offset of α in the fast time direction, which corresponds to the fixed slant-range registration error calculated as $\Delta R = c\alpha/2$. Obviously, this range registration error induced by α will cause the radar echo data decorrelating between the main satellite and auxiliary satellite, that is

$$\rho_{reg\_r} = \mathrm{sinc}\left(\rho_{ct} \cdot \frac{\Delta R}{c/\left(2B\right)} \right) \tag{72}$$

where ρ_{ct} is given in (69). In addition, the fixed time synchronization error will lead to an extra fixed phase error, i.e., $\exp\left\{-j2\pi f_0 \alpha\right\}$, which can be well balanced by using the channel equalization technology [51].

2) Linear time synchronization error

For the same reason, after range compression, the echo signal of the *n*th channel, $n = 1, 2, ..., N$, in the auxiliary satellite can be expressed as

$$\begin{aligned} s_{r,n}(t,t_m) = \sigma rect\left(\frac{t_m + \left(n-1\right)d + B_y \big/ 2V_a}{T_a} \right) \\ \times \mathrm{sinc}\left\{ B\left[t - 2R\left(t_m\right)/c - \beta t_m \right] \right\} \\ \times \exp\left[-j4\pi f_0 R\left(t_m\right)/c \right] \exp\left(-j2\pi f_0 \beta t_m\right) \end{aligned} \tag{73}$$

From (73), one can see that the linear time synchronization error leads to the t_m-related deviation βt_m of the peak value along range dimension. Besides, the linear time synchronization error will also introduce a linear phase term, i.e., $\exp\left\{-j2\pi f_0 \beta t_m\right\}$, causing the Doppler spectrum offset.

G. Influence of Frequency Synchronization Error on Echo Correlation

The frequency error between the different frequency sources of two satellites will lead to the inconsistency between the transmitting carrier frequency and the receiving local oscillator, introducing the phase errors between main and auxiliary radar data. In addition, the instability of frequency source will also cause the phase error, reducing the interchannel coherence.

Consider that the carrier frequency and the local oscillator have the same nominal frequency, and the time-varying frequencies of the carrier frequency and the local oscillator are, respectively, denoted by $\alpha_T\left(t'\right)$ and $\alpha_R\left(t'\right)$.

The transmitting carrier frequency of the main satellite and the local oscillator frequency are, respectively, noted as

$$f_T = f_0 + \alpha_T\left(t'\right) \tag{74}$$

$$f_R = f_0 + \alpha_R\left(t'\right) \tag{75}$$

where $\alpha_i(t') = a_i + b_i t' + \delta(t'), i \in \{T, R\}$, t' represents the whole-time, a_i is the fixed frequency synchronization error, $b_i t'$ denotes the linear frequency synchronization error, and b_i corresponds to the long-term stability index. Due to the short working time of each radar startup, the influence of aging rate can be ignored during a short period of time and the accumulated frequency deviation caused by frequency source aging can be concluded into the fixed frequency error [65]. $\delta(t')$ represents the random frequency error caused by various electrical noises, whose magnitude is usually described by Allen variance [65].

Considering that the linear frequency synchronization error and random frequency synchronization can be ignored, in the following, we mainly analyze the influence of the fixed frequency synchronization error. Then, the transmitted carrier frequency of the main satellite and local oscillator frequency can be approximated as

$$f_T \approx f_0 + \alpha_T \tag{76}$$

$$f_R \approx f_0 + \alpha_R \tag{77}$$

After performing the post-Doppler localization, the echo signal of the auxiliary satellite can be expressed as

$$\begin{aligned} s_R(t, f_a) = \sigma rect\left(\frac{t_m + \left(n-1\right)d + B_y \big/ 2V_a}{T_a} \right) \\ \times \mathrm{sinc}\left[B\left(t - \frac{2R_0}{c} - \frac{\left(\alpha_R - \alpha_T\right)}{K} \right) \right] \\ \times \exp\left(-j\pi \frac{\left(\alpha_R - \alpha_T\right)^2}{K} \right) \exp\left(-j4\pi \frac{\left(f_0 + \alpha_R\right)}{c} R_0 \right) \\ \times \sin c\left\{ T_a \left[f_a - \frac{2\left(f_0 + \alpha_R\right)}{c} V_a \cos\theta_{cone} + \left(\alpha_R - \alpha_T\right) \right] \right\} \end{aligned} \tag{78}$$

It can be seen from (78) that, the fixed frequency synchronization error leads to the fast-time deviation of $\frac{\left(\alpha_R - \alpha_T\right)}{K}$ and the corresponding slant-range synchronization error can be calculated as $\Delta R = \frac{c}{2} \cdot \frac{\left(\alpha_R - \alpha_T\right)}{K}$. In addition, the fixed frequency synchronization error will also introduce the azimuth registration error of

$\left[-\frac{2\alpha_R}{c}V_a\cos\theta_{cone}+(\alpha_R-\alpha_T)\right]\cdot\frac{\lambda R_s}{2V_a}$ and a constant phase error term $\exp\left\{-j\pi\frac{(\alpha_R-\alpha_T)^2}{K}\right\}$.

IV. Simulation Experiments

In this section, the output SCNR of an air moving target and MDV performance are used as the performance indicators to analyze the influences of ATB, CTB, interchannel amplitude/phase error, space synchronization error, time synchronization error, and frequency synchronization error on AMTI. In this simulation, an L-band DSBR system including two satellites is considered, and some of the radar system parameters can be referred to the American large L-band space-based radar system (LLSBR) system, as listed in Table II, III and IV [54].

TABLE Ⅱ
RADAR SYSTEM PARAMETERS

Parameters	Value
Satellite number	2
Number of channels of single satellite	2
ATB length	200 m
Platform altitude	506 km
Carrier frequency	1.26 GHz
Pulse repetition frequency	4000 Hz
Average radiated power	4000 W
Signal bandwidth	3 MHz
Coherent integration time	60 ms
System noise	5 dB
Inclination angle of antenna	45°

TABLE III
ANTENNA PARAMETERS

Parameters	Value
Antenna length	20m
Antenna height	1m
Weighting along elevation dimension	20dB (Taylor window)
Weighting along azimuth dimension	40dB (Taylor window)

TABLE IV
TARGET PARAMETERS

Parameters	Value
RCS	$5m^2$
Elevation angle of the target	40°
Azimuth angle of the target	90°

In order to calculate the MDV value of a moving target, the SCNR detection threshold should be firstly given. Supposing that the scattering model of an observed target obeys the Swerling 0 model, and then the relationship of false alarm probability P_{fa} and detection probability P_d can be given by [66]

$$P_d \approx 0.5\times erfc\left(\sqrt{-\ln P_{fa}}-\sqrt{SNR+0.5}\right) \quad (79)$$

where *SNR* denotes the target signal to noise ratio (SNR).

According to (79), Fig. 5 exhibits the relationship between the detection probability and the SNR in the case of P_{fa} being 10^{-6}. It can be seen from the figure that when the reliable detection probability is up to 0.7, the output SCNR threshold is calculated as 12.1 dB. In the following analysis, this SCNR detection threshold is used to test the moving target detection performance.

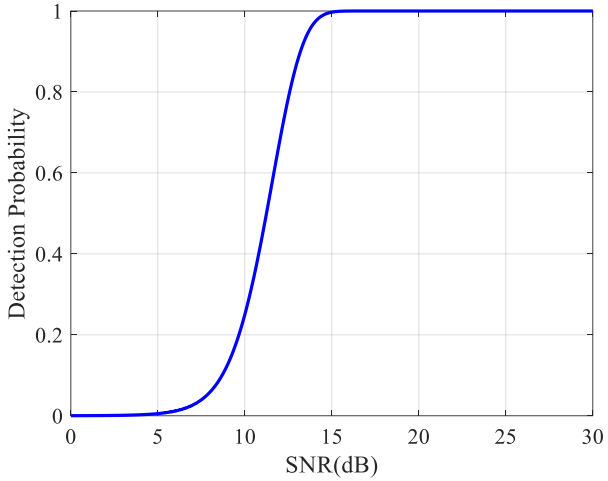

Fig. 5 Detection probability versus with SNR with the P_{fa} of 10^{-6}.

A. Target Velocity Response Analysis with the Presence of ATB

Fig. 6 shows the range-Doppler spectrum of the clutter returns after performing the range and azimuth compressions, from which it can be seen that the clutter spectrum is significantly broadened and mainly concentrated in the main-lobe Doppler regions. It indicates that the moving targets located at the main-lobe regions will be severely submerged by the strong clutter components. Therefore, in order to improve the moving target detection performance, especially for moving targets in the main-lobe clutter regions, the effective clutter rejection becomes necessity.

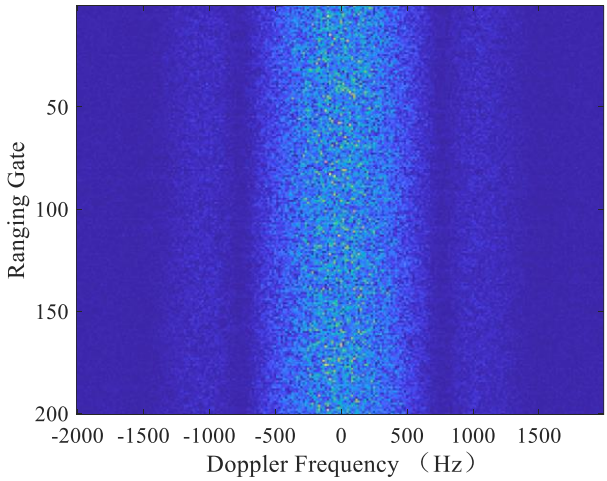

Fig. 6 Range-Doppler spectrum of clutter returns after range and azimuth compressions.

Fig. 7(a) exhibits the echo correlation coefficient between two channels in the main satellite, which is influenced by the channel noise and ATB length. It is noted that ATB length between two channels in the main satellite is only 10 m according to the system parameters in Table Ⅲ and the interchannel correlation coefficient only effected by ATB can be calculated as 0.9997 according to Fig. 2. Thus, the echo correlation coefficient between two channels in the main

satellite is mainly determined by CNR. Fig. 7(b) shows the correlation coefficient between the first channel in the main satellite and the first channel in the auxiliary satellites, which is effected by the channel noise and long ATB between two satellites. It can be seen from the figures that, the theoretically calculated correlation coefficient curve is almost coincided with that counted from the simulated data. As for the spatial filtering notch regions, due to the low clutter energy, the CNR statistic error becomes larger, causing a large deviation between the theoretically calculated correlation coefficient and the actual value. In addition, comparing Fig.7 (a) with Fig.7 (b), one can see that, due to the registration error caused by the long along-track distance between the main satellite and auxiliary satellite, the correlation coefficient decreases to 0.6 times than that of the single satellite.

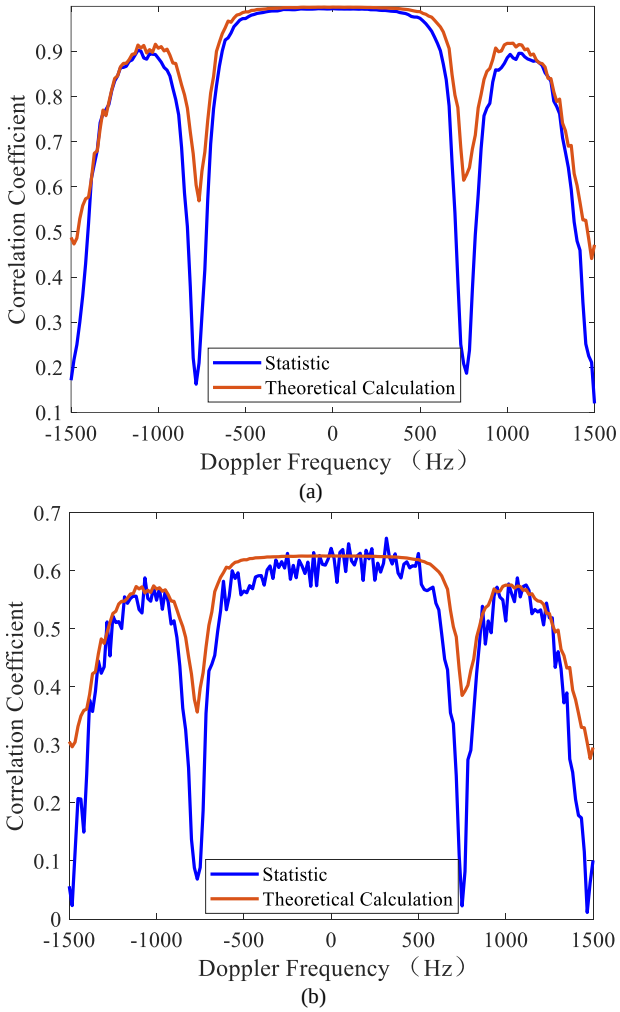

Fig. 7 Correlation coefficient. (a) Correlation coefficient of the first and second channels in the main satellite. (b) Correlation coefficient between the first channel in the main satellite and the first channel in the auxiliary satellite.

Fig. 8 shows the target output SCNR of the single-platform SBEWR system and the DSBR system after clutter suppression by using the extended factor approach (EFA) [18]. It can be seen from the figure that the target output SCNR of a distributed system increases by 3dB compared with that of a single-platform system. In addition, compared with the single-platform system, due to the more receiving spatial channels and longer ATBs, the MDV is improved from 72.31 m/s to 4.02 m/s, which indicates that the DSBR system can significantly improve the MDV performance of an air moving target. However, for the sparsity configuration of distributed antenna array, the antenna pattern exhibits the severe grating effect, resulting in the target discontinuous detectable phenomenon. It should be noted that the grating influences in the side-lobe clutter regions are relatively small because of the transmitted/received antenna pattern modulation.

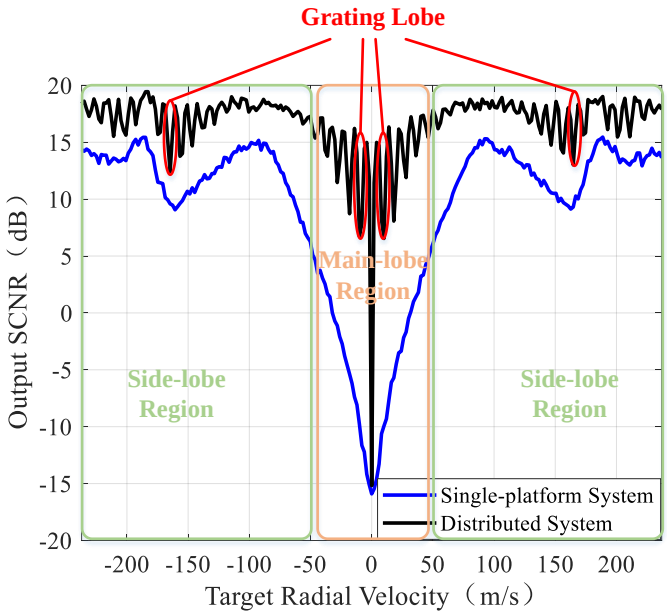

Fig. 8 Output SCNR comparison of a moving target in the single-platform SBEWR system and the DSBR system after clutter suppression by using EFA.

B. Target Velocity Response Analysis with the Presence of CTB

According to (49) and (24), it is observed that the CTB will lead to the ground scattering spectrum deviation between the main and auxiliary satellites, causing the radar returns of two satellites decorrelating. Additionally, the existence of CTB will cause the non-stationary peculiarity of the auxiliary clutter returns, degrading the clutter suppression performance.

Fig. 9 shows the output SCNR of an air moving target, where Case 1 represents the condition that the CTB does not exist (ATB length is 200 m) and Case 2 refers to a DSBR system with an ATB of 200 m and a CTB of 400 m [57]. In this simulation, only the effect of ground scattering spectrum deviation is considered. From the figure, one can see that due to the decorrelation influence of CTB, the clutter suppression capability of the distributed system in Case 2 severely degrades, causing the spatial filtering notch broadening and MDV is degraded from 4.02 m/s (see Fig. 8) to 32.14 m/s.

Accepted Manuscript
Version of record at: https://doi.org/10.1109/TGRS.2022.3202567

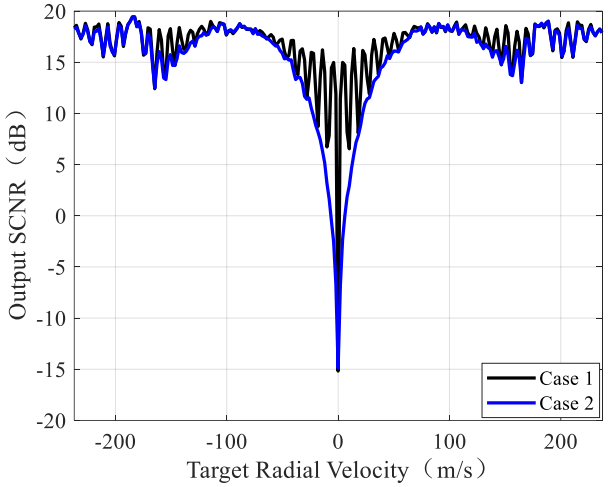

Fig. 9 Target output SCNR. Case 1: the DSBR system only with an ATB of 200m. Case 2: the DSBR system with an ATB of 200 m and a CTB of 400 m (only the effect of ground scattering spectrum deviation is considered).

Fig. 10(a) shows the interferometric phase between the first channel of the main satellite and the first channel of the auxiliary satellite without the consideration of CTB and Fig. 10(b) depicts the corresponding interferometric phase between these two satellite's radar returns with the consideration of CTB. From the figures, it is observed that due to the existence of CTB, the interferometric fringes between two satellites are tilted, indicating that the interferometric phase varies along range dimension. Thus, the i.i.d. characteristics of clutter samples are severely damaged, degrading the subsequent clutter rejection performance.

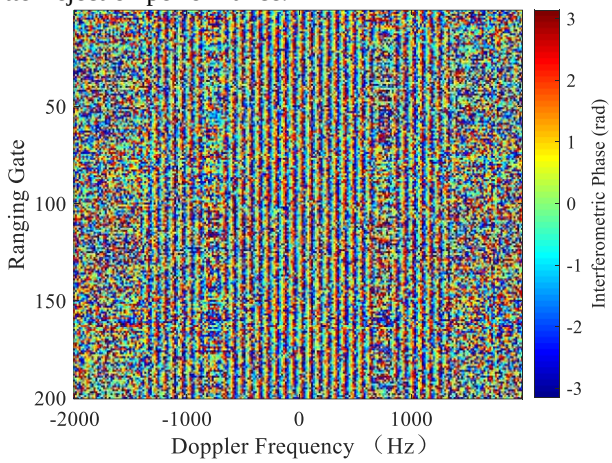

(a)

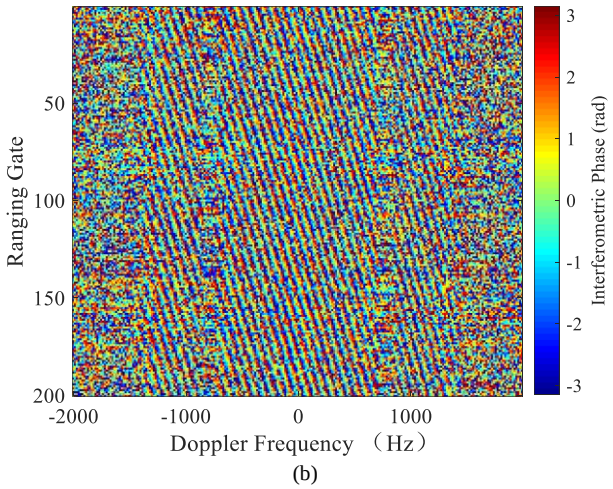

(b)

Fig. 10 Interferometric phase between the first channel of the main satellite and the first channel of the auxiliary satellite. (a) Interferometric phase without the consideration of CTB. (b) Interferometric phase with consideration of CTB.

With the coexistence of CTB (400 m) and ATB (200 m) in a DSBR system, Fig. 11 shows the target output SCNR in two cases, where only the decorrelation effect caused by ground scattering spectrum deviation is considered in Case 1 and both the decorrelation effect caused by ground scattering spectrum deviation and clutter non-stationarity is considered in Case 2. Obviously, with the presence of the flat-ground interferometric phase introduced by CTB (refers to Case 2), the filtering notch is further widened and the target output SCNR decreases by about 1~2dB (MDV ulteriorly deteriorates from 32.14 m/s (see Fig. 9) into 44.19 m/s).

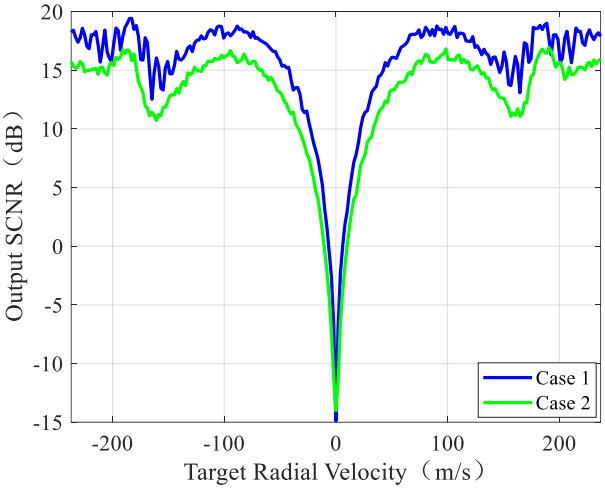

Fig. 11 Target output SCNR in a DSBR system with an ATB of 200 m and a CTB of 400 m. Case 1: Target output SCNR only considering the effect of ground scattering spectrum deviation. Case 2: Target output SCNR where the decorrelation effects caused by ground scattering spectrum deviation and the clutter non-stationary property are both taken into account.

Fig. 12 exhibits the target output SCNR with the CTB length of 100 m, 400 m, and 600 m in a DSBR system (ATB length is 200 m), respectively, in which both the decorrelation effect caused by ground scattering spectrum deviation and clutter non-stationarity are considered. Obviously, the AMTI performance deteriorates with the increase of the CTB length. From the figure, one can see that MDV is degraded from 4.02 m/s (see Fig. 8) to 7.22 m/s. In addition, when the CTB length

increases to be 400 m and 600 m, and the MDVs deteriorate to be 44.19 m/s and 58.25 m/s, respectively.

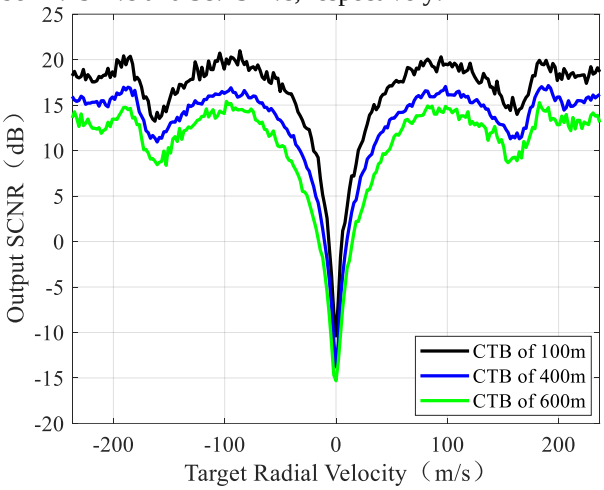

Fig. 12 Target output SCNR in a DSBR system with the CTB length of 100 m, 400 m, and 600 m in a DSBR system (ATB length is 200 m).

Furthermore, according to the analysis results in Section II, it is known that the CTB is sensitive to the terrain elevation. In the following, the influences of the terrain fluctuation on interference phase and moving target detection performance in a DSBR system with the coexistence of CTB (400 m) and ATB (200 m) are analyzed.

Fig. 13(a) shows the interferometric phase between the first channel of the main satellite and the first channel of the auxiliary satellite without the consideration of terrain fluctuation, while Fig. 13(b) with the terrain fluctuation variance of 100 m. From the figures, it can be seen that, due to the existence of random terrain fluctuation, the interferometric fringes present the fluctuating phenomenon and do not appear as strict diagonal lines, indicating that the echo phase distribution is randomly disrupted.

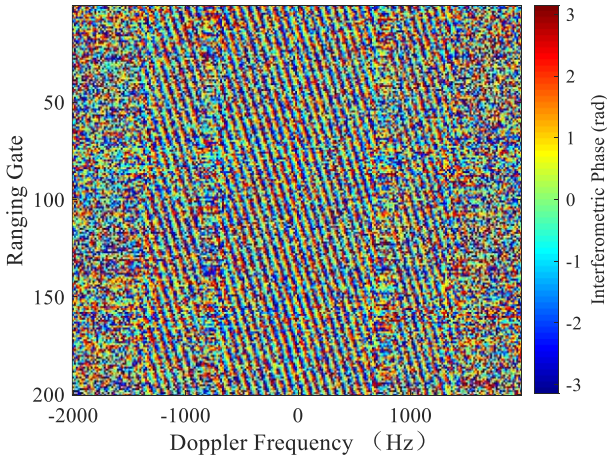

(a)

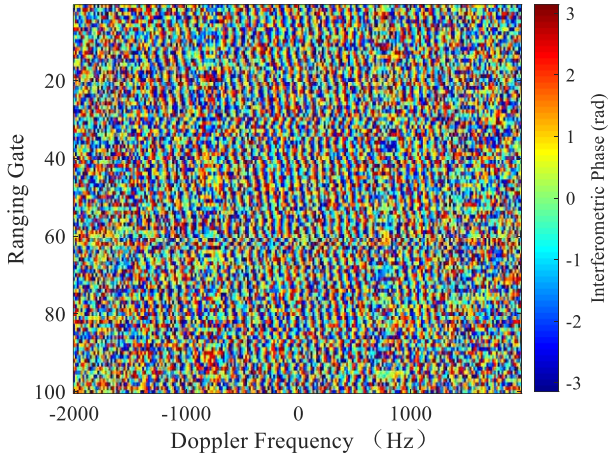

(b)

Fig. 13 Interference phase between the first channel of the main satellite and the first channel of the auxiliary satellite in a DSBR system with an ATB of 200 m and a CTB of 400 m. (a) Interference phase without the consideration of terrain fluctuation. (b) Interference phase with the terrain fluctuation variance of 100 m.

Fig. 14 exhibits the target output SCNR results in a DSBR with the random terrain fluctuation of 0 m (only the flat terrain is present), 10 m, 100 m and 500 m, respectively. As analyzed in Section II, the CTB is sensitive to the terrain, and thus the topographic fluctuation further destroys the i.i.d. property of the training samples, which will ulteriorly degrade the AMTI performance. Table V shows the MDV results with the presence of terrain fluctuation. It can be seen from the figure and the table that, due to the random elevation interferometric phase influence, the larger the random terrain fluctuation, the wider the filtering notch as well as the worse target detection ability in the main-lobe clutter regions.

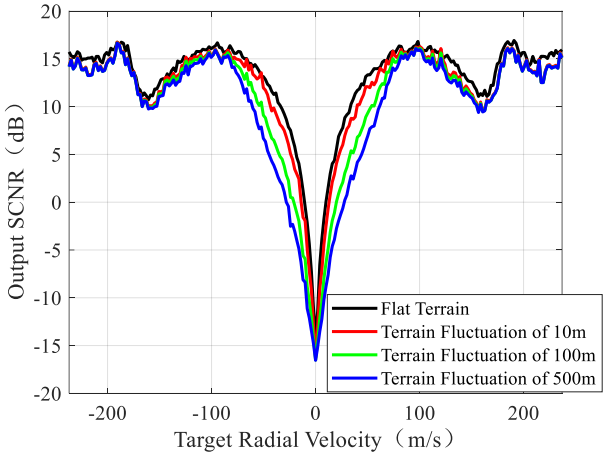

Fig. 14 Target output SCNR curves with the random terrain fluctuation of 0 m (flat terrain), 10 m, 100 m and 500m in a DSBR system with an ATB of 200 m and a CTB of 400 m.

TABLE V
MDV RESULTS WITH THE PRESENCE OF TERRAIN FLUCTUATION

Variance of random terrain fluctuation (m)	0	10	100	500
MDV results (m/s)	44.19	52.22	62.26	70.3

C. Target Velocity Response Analysis with the Presence of Interchannel Amplitude and Phase Error

In this section, in order to quantitatively analyze the influences of interchannel amplitude and phase errors, the random interchannel amplitude and phase errors are added

into a distributed radar system with ATB of 200 m, respectively. Fig. 15 exhibits the target output SCNR with the variance of interchannel amplitude errors setting as 0 dB, 0.1 dB, 0.2 dB, 0.5 dB, 1 dB and 2 dB, respectively. Besides, Table VI gives the MDV statistics results with the consideration of the interchannel amplitude errors. From the figure and table, one can see that if the amplitude error is less than 0.2 dB, the impact of the amplitude error can be ignored.

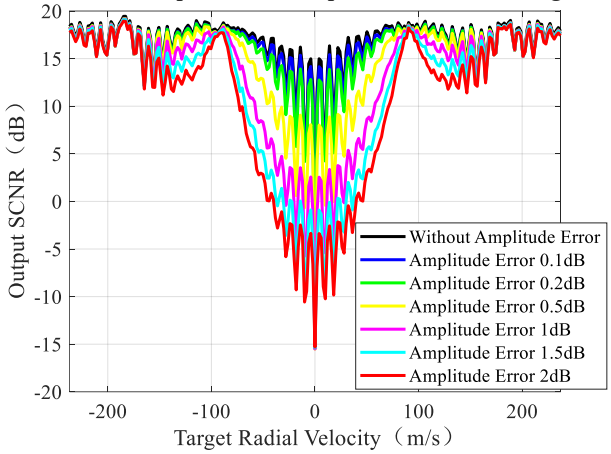

Fig. 15 Target output SCNR under different interchannel amplitude errors (interchannel phase error is not considered).

TABLE VI
MDV RESULTS WITH THE PRESENCE OF INTERCHANNEL AMPLITUDE ERRORS

Amplitude errors (dB)	0	0.1	0.2	0.5	1	1.5	2
MDV results (m/s)	4.02	4.02	4.02	50.21	66.28	72.31	76.32

Fig. 16 shows the target output SCNR and Table VII calculates the MDV with the variance of interchannel phase error setting as 0°, 1°, 2°, 5° and 10°, respectively. It is observed that if the random phase error is less than 2°, the AMTI performance is almost unaffected. However, the spatial filtering notch becomes wider and wider with the increase of the phase error, causing the target MDV performance deteriorates dramatically. Thus, the channel equalization should be operated before clutter suppression.

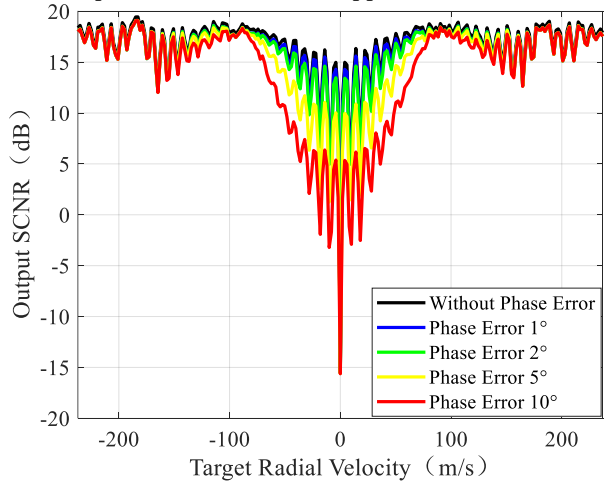

Fig. 16 Target output SCNR under different interchannel phase errors (interchannel amplitude error is not considered).

TABLE VII
MDV RESULTS WITH THE PRESENCE OF INTERCHANNEL PHASE ERRORS

Phase errors (°)	0	1	2	5	10
MDV results (m/s)	4.02	4.02	4.02	32.14	58.25

D. Target Velocity Response Analysis with the Presence of Space Synchronization Error

In this subsection, taking the space synchronization error associated with auxiliary satellite radar for example, the influence of the yaw angle error, pitch angle error, and roll angle error will be analyzed, respectively.

1) Influence of yaw angle error

As analyzed in Section III, the existence of yaw angle error will lead to Doppler center deviation, introducing the azimuth registration error. Furthermore, the yaw angle error will also cause the clutter echoes exhibiting the range dependence.

In the following, the AMTI performances with yaw angle errors of 0°, 0.001°, 0.002°, 0.003°, 0.005° and 0.01° are, respectively, provided in Fig. 17, where the ATB length is 200 m. It can be seen from the figure that if yaw angle error is less than 0.003°, the target output SCNR almost coincides with that of the ideal case, indicating that the influence of yaw angle error can be ignored. However, when the yaw angle error is larger than 0.003°, due to the increased registration error and the severe nonstationary phenomenon of training samples, the clutter cancellation performance and the MDV of an AMT gradually deteriorate with the increasing of yaw angle error. When the yaw angle error does not exist, the MDV is counted as 4.02 m/s. However, when the yaw angle error reaches 0.005°, the MDV is up to 30.13 m/s, while the MDV further deteriorates to be 32.14 m/s when the yaw angle error is 0.01°. Therefore, in order to improve the AMTI performance of a DSBR system, the registration error and range dependence between the main satellite and the auxiliary satellite should be precisely compensated.

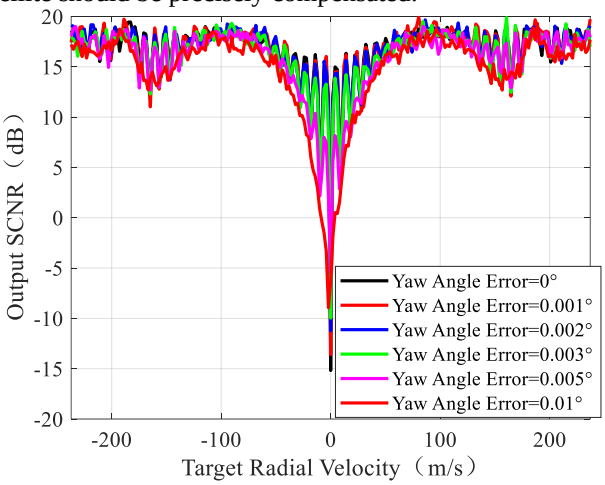

Fig. 17 Target output SCNR with the consideration of yaw angle error in a DSBR system with an ATB of 200 m.

2) Influence of pitch angle error

Similar to the influence of yaw angle error, from the analysis in Section III, it is known that the pitch angle error will also cause the registration error and range dependence between the main and auxiliary satellites. In the following, the pitch angle errors of 0°, 0.001°, 0.002°, 0.003°, 0.004°, 0.005° and 0.01° in a DSBR system are considered, respectively, where the ATB is set as 200 m. From the target output SCNR curve in Fig. 18 and MDV statistics in Table VIII, one can see that if the pitch angle error is less than

Accepted Manuscript
Version of record at: https://doi.org/10.1109/TGRS.2022.3202567

0.003°, the AMTI performance is almost unaffected. Otherwise, the target spatially filtering notch is significantly broadened when the pitch angle error is further increased, exhibiting the poor AMTI performance in the main-lobe clutter region.

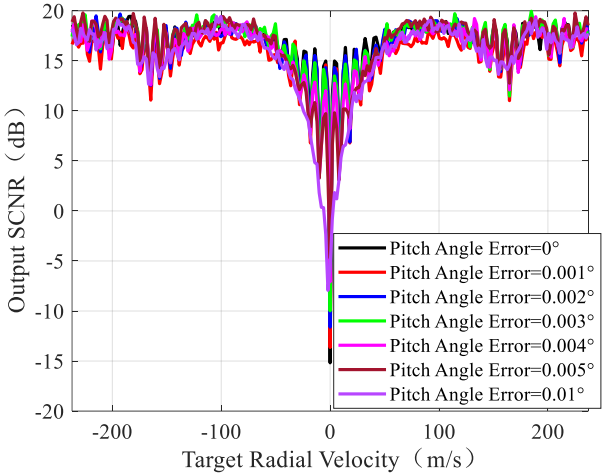

Fig. 18 Target output SCNR with the consideration of pitch angle error in a DSBR system with an ATB of 200 m.

TABLE VIII
MDV RESULTS WITH THE PRESENCE OF PITCH ANGLE ERRORS

Pitch angle errors (°)	0	0.001	0.002	0.003	0.004	0.005	0.01
MDV results (m/s)	4.02	4.02	4.02	4.02	14.06	24.1	32.14

3) Influence of roll angle error

Different from the yaw and pitch angle errors, the roll angle error will not lead to the Doppler center offset to destroy the clutter i.i.d. property. However, the roll angle error will introduce an elevation angle deviation between the main and auxiliary satellites, causing the surface feature scattering spectra offset between two satellites. Fig. 19 shows the target output SCNR and Table IX calculates the MDV with the roll angles setting as 0°, 0.001°, 0.005° and 0.02°, respectively, where the ATB is 200 m. It can be seen from figure that with the increase of the roll angle error, the coherence between the satellite and auxiliary satellites rapidly decreases.

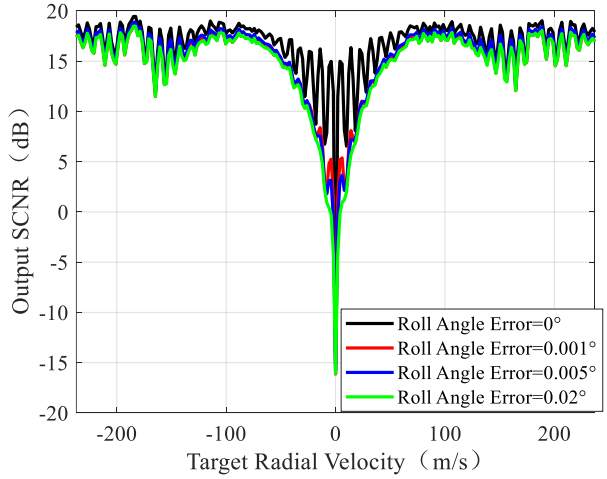

Fig. 19 Target output SCNR with a roll angle error of 0°, 0.001°, 0.005° and 0.02° in a DSBR system (the ATB is set as 200 m).

TABLE IX
MDV RESULTS WITH THE PRESENCE OF ROLL ANGLE ERRORS

Roll angle errors (°)	0	0.001	0.005	0.02
MDV results (m/s)	4.02	32.14	32.14	32.14

E. Target Velocity Response Analysis with the Presence of Time Synchronization Error

The influence of time synchronization error has been theoretically discussed in Section III. It is known that the time synchronization error will introduce a registration error in the range and azimuth dimensions.

Fig. 20 shows the correlation coefficient between the main satellite and auxiliary satellite when only the time synchronization error is considered. Usually, the precision of time synchronization based on GPS can be up to 50 ns [66][68]. From the figure, one can see that if the fixed synchronization error is less than 5×10^{-8} s, the correlation coefficient between two satellites is better than 0.955. Besides, from Fig. 20(b), it is observed that when the linear synchronization error index is not larger than 5×10^{-8}, the linear synchronization error influence can be ignored.

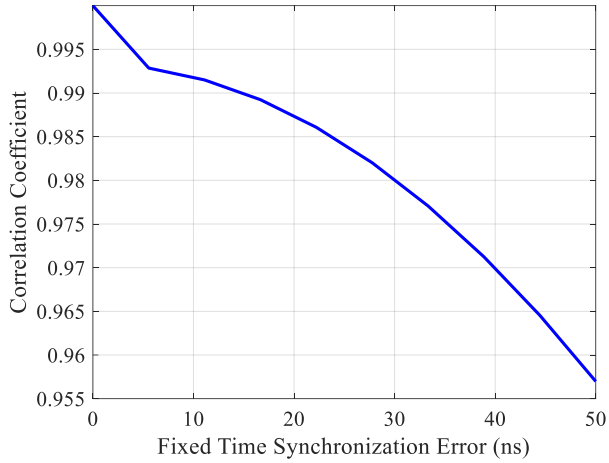

(a)

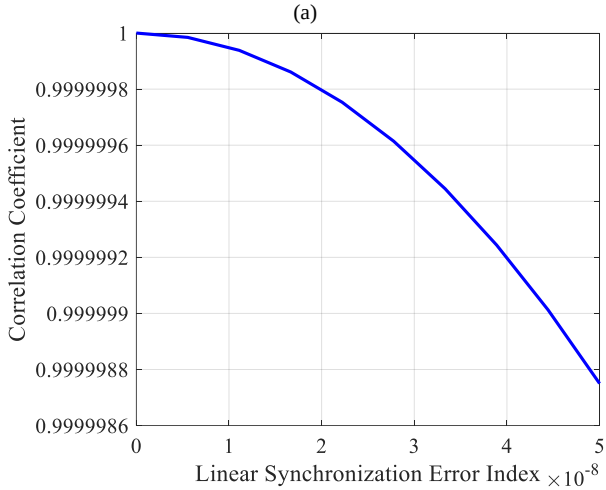

(b)

Fig. 20 Correlation coefficient between the main satellite and auxiliary satellite only with the consideration of time synchronization error. (a) Relationship between the correlation coefficient and the fixed time synchronization error. (b) Relationship between the correlation coefficient and the linearly varied time synchronization error.

Fig. 21 exhibits the target output SCNR in a DSBR system with an ATB of 200 m, where two simulation cases are analyzed: Case 1) the time synchronization error is not

considered; and Case 2) a fixed time synchronization error of 5×10^{-8} s and linear synchronization error index of 5×10^{-8} is taken into account. Obviously, due to the decrease of the correlation coefficient between the main satellite and auxiliary satellite, the AMTI capability degrades severely. From the figure, it is seen that the MDV of an AMT deteriorates from 4.02 m/s to be 32.14 m/s with a fixed time synchronization error of 5×10^{-8}s and linear synchronization error index of 5×10^{-8}, which in turn indicates that a higher-precision demand on the time synchronization error control in a DSBR system is required.

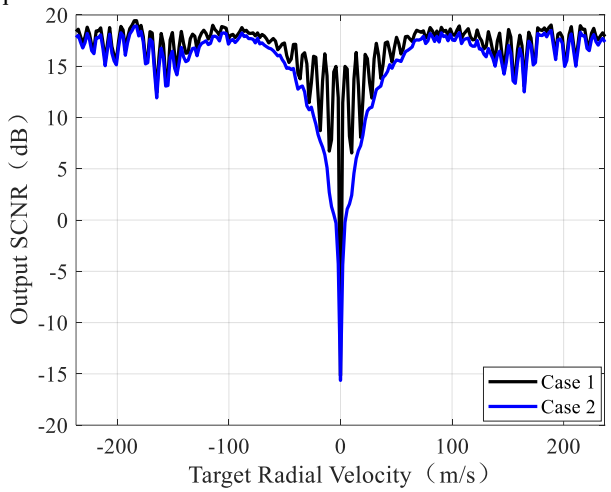

Fig. 21 Target output SCNR in a DSBR system with an ATB of 200 m. Case 1: target output SCNR without the consideration of time synchronization error. Case 2: target output SCNR with a fixed synchronization error of 5×10^{-8}s and the linear synchronization error index of 5×10^{-8}.

F. Target Velocity Response Analysis with the Presence of Frequency Synchronization Error

Similar to the time synchronization error, the frequency synchronization error will also introduce a registration error along range and azimuth dimensions. The influence of the frequency synchronization error on the correlation coefficient and AMTI performance will be analyzed in the following.

Fig. 22 shows the correlation coefficient between the main satellite and auxiliary satellite with a fixed frequency synchronization error. Obviously, the correlation coefficient between two satellites decreases with the increase of fixed frequency synchronization error. Taking the synchronization error of the well-known Tandem-X system [58] for example, the frequency consistency index of the crystal oscillator can reach the level of 10^{-8} [62], which will introduce the fixed frequency synchronization error of about 13 Hz under the system parameters listed in Table I. From the figure, one can see that, the correlation coefficient between the two satellites is better than 0.99 when the fixed frequency synchronization error is smaller than 13 Hz.

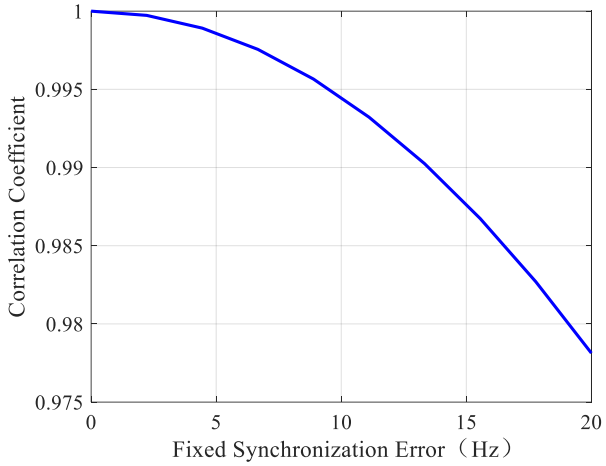

Fig. 22 Correlation coefficient between the main satellite and auxiliary satellite only with the consideration of time synchronization error.

Fig. 23 compares the target output SCNRs in a DSBR system with the frequency synchronization error of 0 Hz and 13Hz (the ATB is 200 m). Obviously, when the level of frequency consistency index is 10^{-8}, the target output SCNR is severely decreased compared with the ideal case and the MDV is increased from 4.02m/s to 30.13 m/s. Therefore, in order to achieve a better AMTI performance, the higher-precision compensation performance of the frequency consistency index error in a crystal oscillator is required.

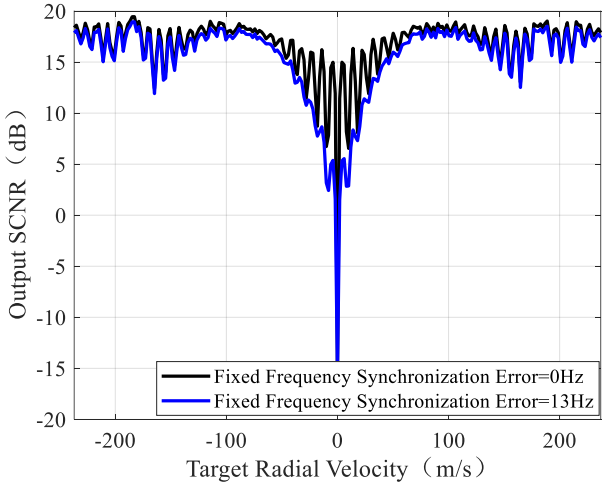

Fig. 23 Target output SCNR in a DSBR with the consideration of frequency synchronization error (the ATB is 200 m).

IV. Conclusions

In this paper, a multi-channel echo signal model of target and clutter in a DSBR system is firstly established, and then several non-ideal error factors are considered, such as noise decorrelation, ATB decorrelation, CTB decorrelation, synchronization errors, and interchannel amplitude/phase errors. Experimental results show that the existence of range registration error introduced by the time and frequency synchronization errors and the azimuth registration error caused by the intersatellite ATB, yaw angle error, pitch angle error, time synchronization error, and frequency synchronization error will decrease the correlation coefficient between the main satellite and auxiliary satellite, and thus the AMTI performance will significantly deteriorate. In order to achieve better AMTI performance of a DSBR system, the

registration error along the range and azimuth dimensions should be accurately compensated before implementing the subsequent spatial digital beamforming techniques. In addition, CTB and roll angle error will both lead to the ground scattering spectrum deviation associated with the radar echoes of two satellites, reducing the intersatellite coherence. At the same time, the presence of CTB, yaw angle error, and pitch angle error, will all cause the clutter exhibiting the severe range-dependence and terrain-dependence, severely destroying i.i.d. characteristics of clutter samples. In addition, the larger the interchannel amplitude and phase errors, the lower the interchannal correlation.

The above analysis provides some important guidance and references for the formation configuration and constraint designs of a new-generation DSBR system with the AMTI working mode. How to further compensate the above-mentioned system errors with high-precision and high-efficiency will be under our future investigation.

REFERENCES

[1] L. L. Yin, W. M. Tian, Z. H. Wang, T. Zeng, and M. K. Mei, "Coupling signal suppression method of ground-based synthetic aperture radar based on singular value decomposition," in *CIE Int. Conf. Radar*, *RADAR*, Guangzhou, China, 2016.

[2] M. C. Chim and D. Perissin, "Application of ground based radar system in structural monitoring," in *Dig Int Geosci Remote Sens Symp (IGARSS)*, Beijing, China, 2016, pp. 6114-6116.

[3] J. Su, G. N. Cui, T. Li, Y. F. Fan, M. L. Tao, H. T. Wang, and X. Zhang, "A Novel Multi-Scan Joint Method for Slow-Moving Target Detection in the Strong Clutter via RPCA," in *Dig Int Geosci Remote Sens Symp (IGARSS)*, Brussels, Belgium, 2021, pp. 4787-4789.

[4] I. Arias and V. Chandrasekar, "Cross validation of GPM and ground-based radar in Latin America and the Caribbean," in *Dig Int Geosci Remote Sens Symp (IGARSS)*, 2018, pp. 3891-3893.

[5] J. Wang, X. D. Liang, L. Y. Chen, L. N. Wang, and K. L., "First Demonstration of Joint Wireless Communication and High-Resolution SAR Imaging Using Airborne MIMO Radar System," *IEEE Trans. Geosci. Remote Sens.*, vol. 57, no. 9, pp. 6619-6632, Sept. 2019.

[6] X. D. Meng, T. Wang, J. X. Wu, and B. Zheng, "Short-range clutter suppression for airborne radar by utilizing prefiltering in elevation," *IEEE Trans. Geosci. Remote Sens.*, vol. 6, no. 2, pp. 268-272, Apr. 2009.

[7] E. Simonetto, H. Oriot, and R. Garello, "Rectangular building extraction from stereoscopic airborne Radar images," *IEEE Trans. Geosci. Remote Sens.*, vol. 43, no. 10, pp. 2386-2395, Oct. 2005.

[8] W. Maurice. *Airborne Early Warning System Concepts*. Artech House, Boston, 1992.

[9] X. Zhang, L. R. Zhang, S. Y. Li, and Y. H. Zhao, "Radar high speed small target detection based on keystone transform and linear canonical transform," *Digit. Signal Prog.*, vol. 82, pp. 203-215, Aug. 2018.

[10] D. N. Fu, J. Wen, J. W. Xu, G. S. Liao, and S. Ouyang, "STAP-based airborne radar system for maneuvering target detection," *IEEE Access*, vol. 7, pp. 62071-62079, Jun. 2019.

[11] L. J. Cantafio. *Space-Based Radar Handbook*. Artech House, Boston, 1989.

[12] T. Iwahashi and H. Tanaka, "Satellite technology for environmental observation," *Mitsubishi Electric Advance*, vol. 74, no. 3, pp. 8-10, Mar. 1996.

[13] D. Hounam, S. Baumgartner, K. H. Bethke, M. Gabele, E. Kemptner, D. Klement, G. Krieger, G. Rode, and K. Wagel, "An autonomous, non-cooperative, wide-area traffic monitoring system using space-based Radar (TRAMRAD) ," in *Dig Int Geosci Remote Sens Symp (IGARSS)*, Seoul, Korea, 2005.

[14] B. Widrow, P. E. Mantey, L. J. Griffiths, and B. B. Goode, "Adaptive antenna system," *Proc. IEEE*, vol. 55, no. 12, pp. 2143-2159, Dec. 1967.

[15] Z. Li, H. Ye, Z. Liu, Z. Sun, H. An, J. Wu, and J. Yang, "Bistatic SAR Clutter-Ridge Matched STAP Method for Non-stationary Clutter Suppression," *IEEE Trans. Geosci. Remote Sens.*, vol. 60, pp. 1-14, 2022, Art no. 5216914.

[16] Z. Li, C. Huang, Z. Sun, H. An, J. Wu, and J. Yang, "BeiDou-Based Passive Multistatic Radar Maritime Moving Target Detection Technique via Space-Time Hybrid Integration Processing," *IEEE Trans. Geosci. Remote Sens.*, vol. 60, pp. 1-13, 2022, Art no. 5802313.

[17] J. Y. Chen, P. H. Huang, X. Z. Liu, G. S. Liao, J. L. Chen, Y. Y. Sun, and G. Z. Chen, "Approach for topography-dependent clutter suppression in a spaceborne surveillance radar system based on adaptive broadening processing," *IEEE Geosci. Remote Sens. Lett.*, to be published. DOI: 10.1109/LGRS.2021.3109261.

[18] J. Ward, *Space-Time Adaptive Processing for Airborne Radar*, No. 1015. London: MIT Lincoln Laboratory, 1994.

[19] H. Wang and L. J. Cai, "On adaptive spatial-temporal processing for airborne surveillance radar systems," *IEEE Trans. Aerosp. Electron. Syst.*, vol. 30, no. 3, pp. 660-670, Jul. 2010.

[20] M. V. Dragoševic, W. Burwash, and S. Chiu, "Detection and estimation with RADARSAT-2 moving-object detection experiment modes," *IEEE Trans. Geosci. Remote Sens.*, vol. 50, no. 9, pp. 3527–3543, Sep. 2012.

[21] N. Cui, K. Q. Duan, K. Xing, and Z. J. Yu, "Beam-space reduced-dimension 3D-STAP for nonside-looking airborne radar," *IEEE. Geosci. Remote Sens. Let.*, to be published. DOI: 10.1109/LGRS.2021.3080291.

[22] R. Klemm. *Principles of Space-Time Adaptive Processing*. London, United Kingdom, 2002.

[23] L. E. Brennan, D. J. Piwinski, and F. M. Staudaher, "Comparison of space-time adaptive processing approaches using experimental airborne radar data," in *1993 Natl Radar Conf*, Lynnfield, MA, USA, 1993, pp. 176-181.

[24] R. C. Dipietro, "Extended Factored space-time processing for airborne radar systems," *Conf. Rec. Asilomar Conf. Signals Syst. Comput.*, Pacific Grove, CA, United states, 1992, pp. 425-430.

[25] H. Wang and L. J. Wang, "On adaptive spatial-temporal processing for airborne surveillance radar systems," *IEEE Trans. Aerosp. Electron. Syst.*, vol. 30, no. 3, pp. 660-670, Jul. 1994.

[26] R. S. Adve, T. B. Hale, and M. C. Wicks, "Practical joint domain localised adaptive processing in homogeneous and nonhomogeneous environments. Part 1: Homogeneous environments," *IEE Proc Radar Sonar Navig*, vol. 147, no. 2, pp. 57-65, Apr. 2000.

[27] R. D. Brown, R. A. Schneible, M. C. Wicks, H. Wang, and Y. H. Zhang, "STAP for clutter suppression with sum and difference beams," *IEEE Trans. Aerosp. Electron. Syst.*, vol. 36, no. 2, pp. 634-646, Apr. 2000.

[28] D. J. Rabideau and A. O. Steinhardt, "Improved adaptive clutter cancellation through data-adaptive training," *IEEE Trans. Aerosp. Electron. Syst.*, vol. 35, no. 3, pp. 879-891, Jul. 1999.

[29] S. M. Kogon and M. A. Zatman, "STAP adaptive weight training using phase and power selection criteria," in *Conf Rec Asilomar Conf Signals Syst Comput*, Pacific Grove, CA, United states, 2001, pp. 98-102.

[30] T. K. Sarkar, H. Wang, S. Park, J. W. Koh, K. J. Kim, Y. H. Zhang, M. C. Wicks, and R. D. Brown, "A deterministic least-squares approach to space-time adaptive processing (STAP)," *IEEE Trans. Antennas Propag.*, vol. 49, no. 1, pp. 91-103, Jan. 2001.

[31] J. R. Roman, M. Rangaswamy, D. W. Davis, Q. W. Zhang, B. Himed, and J. H. Michels, "Parametric adaptive matched filter for airborne radar applications," *IEEE Trans. Aerosp. Electron. Syst.*, vol. 36, no. 2, pp. 677-692, Apr. 2000.

[32] G. K. Borsari, "Mitigating effects on STAP processing caused by an inclined array," in *Proc. IEEE Radar Conf., Challenges Radar Syst. Solutions*, May 1998, pp. 135–140.

[33] B. Himed, Y. Zhang, and A. Hajjari, "STAP with angle-Doppler compensation for bistatic airborne radars," in *Proc. IEEE Radar Conf.*, Apr. 2002, pp. 311–317.

[34] A. Jaffer and P. T. Ho, "Adaptive angle-Doppler compensation techniques for bistatic STAP radars," AFRL-SN-RS-TR-2005-398, AFRL, 2005.

[35] B. Friedlander, "The MVDR beamformer for circular arrays," in *Conf Rec Asilomar Conf Signals Syst Comput*, Pacific Grove, CA, USA, 2002, pp. 1058-6393.

[36] V. Varadarajan and J. L. Krolik, "Joint space-time interpolation for distorted linear and bistatic array geometries," *IEEE Trans. Signal Process.*, vol. 24, no. 3, pp. 848-860, Mar. 2006.

[37] M. Gabele and M. Younis, "Comparison of techniques for future spaceborne GMTI," in *Proc. Eur. Conf. Syn. Aperture Radar*, *EUSAR*, Aachen, Germany, 2010, pp. 386-389.

[38] A. Das, R. Cobb, and M. Stallard, "TechSat 21-A revolutionary concept in distributed space based sensing," in *Def. Civ. Space. Programs. Conf. Exhib.*, Huntsville, AL, 1998, AIAA-98-5255.

[39] M. Martin and M. Stallard, "Distributed satellite missions and technologies-the TechSat 21 program," in *AIAA Space Conf. Expos.*, Albuquerque, NM, 1999, AIAA-99-4479.

[40] C. H. Gierull, D. Cerutti-Maori, and J. Ender, "Ground moving target indication with Tandem satellite constellations," *IEEE Geosci. Remote Sens. Lett.*, vol. 5, no. 4, pp. 710-714, Oct. 2008.
[41] S. Suchandt, M. Eineder, H. Breit, and H. Runge, "Analysis of ground moving objects using SRTM/X-SAR data," *ISPRS-J. Photogramm. Remote Sens.*, vol. 61, no. 3, pp. 209-224, Dec. 2006.
[42] E. Makhoul, S. V. Baumgartner, M. Jager, and A. Broquetas, "Multichannel SAR-GMTI in maritime scenarios with F-SAR and TerraSAR-X sensors," *IEEE J. Sel. Top. Appl. Earth Observ. Remote Sens.*, vol. 8, no. 11, pp. 5052-5067, Nov. 2015.
[43] F. Gatelli, A. M. Guamieri, F. Parizzi, P. Pasquali, C. Prati, and F. Rocca, "The wavenumber shift in SAR inferometry," *IEEE Trans. Geosci. Remote Sens.*, vol. 32, no. 4, pp. 855-865, Jul. 1994.
[44] D. Geudtner, M. Zink, C. Gierull, and S. Shaffer, "Interferometric alignment of the X-SAR antenna system on the space shuttle radar topography mission," *IEEE Trans. Geosci. Remote Sens.*, vol. 40, no. 5, pp. 995-1006, May. 2002.
[45] M. M. Zhang, R. Wang, Y. K. Deng, L. X. Wu, Z. M. Zhang, H. Zhang, N. Li, Y. Liu, and X. L. Luo, "A Synchronization Algorithm for Spaceborne/Stationary BiSAR Imaging Based on Contrast Optimization With Direct Signal From Radar Satellite," *IEEE Trans. Geosci. Remote Sens.*, vol. 54, no. 4, pp. 1977-1989, Apr. 2016.
[46] K. S. Liu, "An analysis of some problems of bistatic and multistatic radars," in *Proc. Int. Conf. Radar, RADAR*, Adelaide, SA, Australia, 2003, pp. 429-432.
[47] M. W. Roth, "High-resolution interferometric synthetic aperture radar for discoverer II," *Johns Hopkins APL Technical Digest*, vol. 20, no. 3, pp. 297-304, Jul. 1997.
[48] G. D. Jin, K. Y. Liu, D. C. Liu, D. Liang, H. Zhang, N. M. Ou, Y. Y. Zhang, Y. K. Deng, C. Li., and R. Wang, "An Advanced Phase Synchronization Scheme for LT-1," *IEEE Trans. Geosci. Remote Sens.*, vol. 58, no. 3, pp. 1735-1746, Mar. 2020.
[49] F. A. Butt, M. A. Aslam, M. T. Zafar, I. H. Naqvi, and U. Riaz, "Synchronization of long-range, widely-separated MIMO radar network using GSM protocol," in *Proc. Int. Radar Symp.*, Bonn, Germany, 2018, pp. 2155-5753.
[50] J. B. Jing, G. C. Sun, X. G. Xia, M. D. Xing, and Z. Bao, "A Novel Two-Step Approach of Error Estimation for Stepped-Frequency MIMO-SAR," *IEEE Geosci. Remote Sens. Lett.*, vol. 14, no. 12, pp. 2290-2294, Dec. 2017.
[51] V. Tocca, D. Vigilante, R. Petrucci, L. Timmoneri, and A. Farina, "Adaptive beam-forming algorithms for active array sensors: An enabling capability for cognitive radars," in *IEEE Int. Workshop Metrol. AeroSpace, MetroAeroSpace - Proc.*, Virtual, Online, 2021, pp. 176-181.
[52] J. H. G. Ender and J. Klare, "System architectures and algorithms for radar imaging by MIMO-SAR," in *IEEE Nat Radar Conf Proc*, Pasadena, CA, United states, 2009.
[53] T. J. Nohara, P. Weber, and A. Premji, "Space-based radar signal processing baselines for air, land and sea applications," *Electronics & Communication Engineering Journal*, vol. 12, no. 5, pp. 229-239, Oct. 2000.
[54] E. D. Mark, "L-band SBR moving target detection in SAR-GMTI modes," in *IEEE Aerosp. Conf. Proc.*, Big Sky, MT, United states, 2004, pp. 2211-2219.
[55] Z. F. Li, Z. Bao, H. Y. Wang, and G. S. Liao, "Performance improvement for constellation SAR using signal processing techniques," *IEEE Trans. Aerosp. Electron. Syst.*, vol. 42, no. 2, pp. 436-452, Apr. 2006.
[56] D. Just and R. Bamler, "Phase statistics of interferograms with applications to synthetic aperture radar," *Appl. Optics*, vol. 33, no. 20, pp. 4361-4368, Jul. 1994.
[57] H. Fiedler, G. Krieger, M. Werner, K. Reiniger, M. Eineder, S. D'Amico, E. Diedrich, and M. Wickler, "The Tandem-X mission design and data acquisition plan," in *Proc. Eur. Conf. Syn. Aperture Radar, EUSAR*, 2006.
[58] A. Moreira, G. Krieger, I. Hajnsek, K. Papathanassiou, M. Younis, P. Lopez-Dekker, S. Huber, M. Villano, M. Pardini, M. Eineder, F. D. Zan, and A. Parizzi, "Tandem-L: A highly innovative bistatic SAR mission for global observation of dynamic processes on the earth's surface," *IEEE Geosci. Remote Sens. Mag.*, vol. 3, no. 2, pp. 8-23, Jun. 2015.
[59] D. Shen, K. Pham, E. Blasch, H. M. Chen, and G. S. Chen, "Pursuit-evasion orbital game for satellite interception and collision avoidance," *Proc. SPIE 8044, Sensors and Systems for Space Applications IV*, 80440B, May. 2011.
[60] G. W. Hill, "Researches in the lunar theory," *Am. J. Math.*, vol. 1, no. 1, pp. 5-26, 1878.
[61] G. Krieger, M. Zink, M. Bachmann, B. Bräutigam, D. Schulze, M. Martone, P. Rizzoli, U. Steinbrecher, J. W. Antony, F. D. Zan, I. Hajnsek, K. Papathanassiou, F. Kugler, M. R. Cassola, M. Younis, S. Baumgartner, P. Lopez-Dekker, P. Prats, and A. Moreira, "TanDEM-X: A radar interferometer with two formation-flying satellites," *Acta Astronaut.*, vol. 89, pp. 83-98, Aug. 2013.
[62] G. Krieger, A. Moreira, H. Fiedler, I. Hajnsek, M. Werner, M. Younis, and M. Zink, "TanDEM-X: A satellite formation for high-resolution SAR interferometry," *IEEE Trans. Geosci. Remote Sens.*, vol. 45, no. 11, pp. 3317-3341, Nov. 2007.
[63] A. J. Weiss and B. Friedlander, "Eigenstructure methods for direction finding with sensor gain and phase uncertainties," *Circuits Syst. Signal Process.*, vol. 9, no. 3, pp. 271-300, Jan. 1990.
[64] F. Sivrikaya and B. Yener, "Time synchronization in sensor networks: A survey," *IEEE Netw.*, vol. 18, no. 4, pp. 45-50, Jul. 2004.
[65] Y. S. Zhang, D. N. Liang, and Z. Dong, "Analysis of time and frequency synchronization errors in spaceborne parasitic InSAR system," in *Dig Int Geosci Remote Sens Symp (IGARSS)*, Denver, CO, United states, 2006, pp. 3047-3050.
[66] D. O. North, "An Analysis of the factors which determine signal/noise discrimination in pulsed-carrier systems," *Proc. IEEE*, vol. 51, no. 7, pp. 1016-1027, Jul. 2963.
[67] H. Khudov, S. Kovalevskyi, A. Irkha, V. Lishchenko, O. Serdiuk, and F. Zots, "The proposals for synchronization positions of MIMO radar system on the basis of surveillance radars," in *IEEE Int. Sci.-Pract. Conf.: Probl. Infocommunications Sci. Technol., PIC S T - Proc.*, Kyiv, Ukraine, 2019, pp. 547-551.
[68] K. Klincewicz, "Demonstrator of the SDR-based multistatic system for localizing different sources of emissions," in *Proc. Int. Radar Symp.*, Krakow, Poland, 2016, pp. 2155-5753.
[69] S. Pavone, I. Zoccali, M. Gabella, and G. Perona, "Measurement simulations from spaceborne weather radar," in *Dig Int Geosci Remote Sens Symp (IGARSS)*, Honolulu, HI, USA, 2000, pp. 530-532.

Jiangyuan Chen received the B.S. degree in electronic and information engineering from Xidian University, Xi'an, China, in 2019. She is working toward the Ph.D. degree with the School of Electronic Information and Electrical Engineering ShanghaiJiao Tong University, Shanghai, China.

Her research interests include space-borne early warning radar system design, distributed space-borne wide-area surveillance radar signal processing with air moving target indication (AMTI), and space-time adaptive processing (STAP).

Penghui Huang (M'17) was born in Jiangxi, China. He received the B.S. and PH.D. degrees in electrical engineering from Xidian University, Xi'an, China, in 2012 and 2017, respectively.

He joined in the School of Electronic Information and Electrical Engineering, Shanghai Jiao Tong University, Shanghai, China, in 2017. He was an Assistant Professor from 2017 to 2021, and he is currently an Associate Professor and a Ph.D adviser. His research interests include space-borne early warning radar system design, space-time adaptive processing (STAP), multi-channel sea clutter modeling, simulation, space-time property analysis, and robust suppression, distributed space-borne wide-area surveillance radar signal processing with ground moving target indication (GMTI) and air moving target indication (AMTI), space-borne HRWS-SAR imaging, ISAR imaging, and weak target detection and tracking. He was the recipient of the Prize for

Excellent Ph.D. degree dissertation of the Chinese Institute of Electronics education in 2017, and also the recipient of the Prize for Excellent Ph.D. degree dissertation of the Shaanxi Province in 2019.

Dr. Huang is a Reviewer of the IEEE Transactions on Geoscience and remote sensing, the IEEE Transactions on Aerospace and Electronic Systems, the IEEE Transactions on Signal Processing, the IEEE Journal of Selected Topics in Applied Earth Observations and Remote Sensing, the IEEE Sensor Journals, the IEEE Geoscience and Remote Sensing Letters, etc.

Xiang-Gen Xia (M'97, S'00, F'09) received his B.S. degree in mathematics from Nanjing Normal University, Nanjing, China, and his M.S. degree in mathematics from Nankai University, Tianjin, China, and his Ph.D. degree in electrical engineering from the University of Southern California, Los Angeles, in 1983, 1986, and 1992, respectively.

He was a Senior/Research Staff Member at Hughes Research Laboratories, Malibu, California, during 1995-1996. In September 1996, he joined the Department of Electrical and Computer Engineering, University of Delaware, Newark, Delaware, where he is the Charles Black Evans Professor. His current research interests include space-time coding, MIMO and OFDM systems, digital signal processing, and SAR and ISAR imaging. Dr. Xia is the author of the book Modulated Coding for Intersymbol Interference Channels (New York, Marcel Dekker, 2000).

Dr. Xia received the National Science Foundation (NSF) Faculty Early Career Development (CAREER) Program Award in 1997, the Office of Naval Research (ONR) Young Investigator Award in 1998, and the Outstanding Overseas Young Investigator Award from the National Nature Science Foundation of China in 2001. He received the 2019 Information Theory Outstanding Overseas Chinese Scientist Award, The Information Theory Society of Chinese Institute of Electronics. Dr. Xia has served as an Associate Editor for numerous international journals including IEEE Transactions on Signal Processing, IEEE Transactions on Wireless Communications, IEEE Transactions on Mobile Computing, and IEEE Transactions on Vehicular Technology. Dr. Xia is Technical Program Chair of the Signal Processing Symp., Globecom 2007 in Washington D.C. and the General Co-Chair of ICASSP 2005 in Philadelphia.

Junli Chen received the B.S. degree from the Harbin Institute of Technology, Harbin, China, in 1996, and the Ph.D. degree in electrical engineering from Shanghai Jiaotong University, Shanghai, China, in 2010.

He is currently a member with the Shanghai Academy of Spaceflight Technology, Shanghai. His research interests include signal processing for spaceborne radar and interferometric synthetic aperture radar (SAR) systems.

Yongyan Sun was born in Shandong, China, in 1978. He received the M.S. degree in computer

application from Shanghai Jiao Tong University, Shanghai, China, in 2008.

He is currently a Research Fellow with the Shanghai Institute of Satellite Engineering, Shanghai. His research interests include satellite general design and optimization technology, spacecraft configuration and layout design, and spacecraft orbit and constellation design in China.

Xingzhao Liu (M’04) received the B.S. and M.S. degrees from Harbin Institute of Technology, Harbin, China, in 1984 and 1992, respectively, and the Ph.D. degree from the University of Tokushima, Tokushima, Japan, in 1995, all in electrical engineering.

He was an Assistant Professor, an Associate Professor, and a Professor with Harbin Institute of Technology, from 1984 to 1998. Since 1998, he has been a Professor with Shanghai Jiao Tong University, Shanghai, China. His research interests include high-frequency radar and synthetic aperture radar signal processing.

Guisheng Liao (M’96~SM’16) was born in Guiling, China. He received the B.S. degree from Guangxi University, Guangxi, China, and the M.S. and Ph.D. degrees from Xidian University, Xi’an, China, in 1985, 1990, and 1992, respectively.

He is currently a Professor with Xidian University, where he is also Dean of School of Electronic Engineering. He has been a Senior Visiting Scholar in the Chinese University of Hong Kong, Hong Kong. His research interests include synthetic aperture radar (SAR), space–time adaptive processing, SAR ground moving target indication, and distributed small satellite SAR system design. Prof. Liao is a member of the National Outstanding Person and the Cheung Kong Scholars in China.